University of Modena and Reggio Emilia

Department of Engineering "Enzo Ferrari"

Master's Degree in Electronic Engineering

Theoretical and Numerical Investigation of Tube-Shape Effects in Hollow-Core Inhibited-Coupling Fibers

Supervisor:

Prof. Luca Vincetti

Dr. Federico Melli

Candidate:

Daniela Trivigno

Academic Year 2025/2026

Contents

1 Introduction **1**

2 Theoretical and Numerical Framework **4**

2.1 Guidance Mechanisms in Optical Fibers 4

2.2 Tube Lattice Fiber Structure 5

2.3 Modal Structure of the Tube Lattice Fiber 7

2.3.1 Core Modes 8

2.3.2 Hole Modes 8

2.3.3 Dielectric Modes 8

2.3.4 Single-Tube Approximation and Dielectric-Mode Cut-Off Frequencies 9

2.4 Confinement Loss: Mode-Coupling Loss and Tube-Tunneling Loss . . 11

2.5 Inhibited-Coupling Mechanism 13

2.6 Azimuthal Fourier Decomposition 16

2.7 Artificial-Index Fiber for MCL Isolation 20

3 Effect of Elliptical Tube Geometry **23**

3.1 Reference and Elliptical Tube Geometries 24

3.2 Numerical Model 25

3.3 Inner-Boundary Curvature Analysis 30

3.4 Mode-Coupling-Loss Analysis 32

3.5 Azimuthal Spectrum of the Fundamental Mode 34

3.6 Dielectric-Mode Cut-Off Frequencies 36

3.7 Combined Interpretation of the FM Azimuthal Spectrum and DM Cut-Offs 39

3.8 Geometrical Interpretation in Terms of Boundary Spatial Wavenumber 42

3.9 Conclusions 45

4 Local Modification of the Core-Facing Tube Apex **47**

4.1 Reference Geometry and Local Modification 48

4.2 Boundary Curvature Analysis 50

4.3 Mode-Coupling-Loss Analysis 53
4.4 Azimuthal Fourier Decomposition of the Fundamental Mode 56
4.5 Dielectric-Mode Cut-Off Frequencies 59
4.6 Combined Interpretation of Mode-Coupling Loss 61
4.7 Conclusions 63

5 Conclusions **65**

List of Figures

2.1 Schematic cross-section of a Tube Lattice Fiber and definition of the main geometrical parameters: core radius R_{co}, tube inner and outer radii r_{int} and r_{ext}, tube-wall thickness t, and inter-tube gap δ. 6

2.2 Representative modal structure of a Tube Lattice Fiber. The upper panel shows the dispersion curves of the Fundamental Core Mode, a Hole Mode, and representative Dielectric Modes. The lower panel shows the corresponding Confinement Loss of the FCM, with alternating High-Loss Regions and Transmission Bands. 7

2.3 Dielectric mode azimuthal index μ and corresponding cut-off frequencies F_c for different values of the radial index ν and tube aspect ratios ρ. Colors indicate the radial order:ν= 1 (red), ν= 2 (blue), ν= 3 (purple), ν= 4 (orange).Empty symbols indicate EH modes and filled symbols indicate HE modes. 10

2.4 Absolute value of the real part of the radial Poynting vector, $|\mathrm{Re}(p_r)|$, for a TLF at $F = 1.25$ and $F = 1.66$. White lines indicate the p_r streamlines. 12

2.5 (a) Cross-sections of Tube Lattice (red), Nested (cyan), Double-Nested (yellow), and Triple-Nested (purple) hollow-core fibers. (b) Confinement-Loss spectra of the corresponding fiber designs shown in (a). 12

2.6 Dispersion and attenuation curves in the weak- and strong-coupling regimes. In weak coupling the dispersion curves cross while the attenuation curves exhibit an anti-crossing; in strong coupling the opposite behavior occurs. 14

2.7 Azimuthal Fourier Decomposition of the Fundamental Core Mode. (a) FCM field distribution in the TLF cross-section, with the inner boundary of the selected tube highlighted in blue. (b) Transverse electric field sampled along this boundary and corresponding squared AFD coefficients $|R_m|^2$. 17

2.8 Azimuthal field profile and corresponding Fourier spectrum of the $EH_{5,3}$ Dielectric Mode. The approximately sinusoidal field distribution gives rise to dominant Fourier components at $m = \pm 5$, corresponding to the azimuthal mode order $\mu = 5$. 18
2.9 Relation between the FCM azimuthal spectrum, the Dielectric-Mode cut-off frequencies, and the corresponding coupling contributions. (a) Squared FCM AFD coefficients $|R_m^{\mathrm{FCM}}|^2$. (b) Cut-off frequencies of EH modes with radial orders $\nu = 2$ and $\nu = 3$. (c) Corresponding squared Azimuthal Spectra Overlap g_{EH}^2. The dashed lines highlight the case $\mu = 4$. 19
2.10 Artificial-index TLF configuration used to isolate Mode-Coupling Loss. The artificial low-index material is introduced inside the tube holes and in the inter-tube regions and is kept at a finite distance from the dielectric tube walls in order to preserve the original modal structure. 20
2.11 Comparison between the Confinement Loss of the original TLF and that of the corresponding "artificial-index" configuration A1. The vertical bars represent the squared Fundamental-Mode AFD coefficients $|R_m|^2$ positioned at the cut-off frequencies of the corresponding Dielectric Modes. 21

3.1 (a) Cross sections of TLF with circular and elliptical tubes. (b) Inner-boundary profiles for different tube axis ratios e. 24
3.2 Cross-section of the eight-tube TLF used in the numerical analysis, showing the main geometrical parameters and the artificial-index regions employed in the A1 configuration. 25
3.3 Computational domains employed in the numerical analysis: (a) quarter cross-section of the complete fiber used for the Fundamental-Mode and loss calculations; (b) half cross-section of the isolated tubular element used for the calculation of the Dielectric-Mode cut-off frequencies. 27
3.4 Inner-boundary curvature κ of the circular and elliptical tube profiles as a function of the normalized curvilinear coordinate s_{norm}. 31
3.5 Mode-Coupling Loss spectra of the circular and elliptical tube geometries as a function of the normalized frequency F. 32
3.6 Normalized-frequency bandwidth enlargement ΔF_{th} at the MCL level of 10^{-2} dB/km with respect to the circular reference, as a function of the tube axis ratio b/a. 33
3.7 Squared normalized AFD coefficients $|\widetilde{R}_m|^2$ of the Fundamental Mode for the circular and elliptical tube geometries at $F = 1.6$. 34

3.8 RMS Fourier order m_{rms} of the Fundamental-Mode azimuthal spectrum as a function of the tube axis ratio b/a. 35
3.9 Azimuthal order m and corresponding normalized cut-off frequency F_c of the EH-polarized Dielectric Modes belonging to the $\nu = 2$ radial family, for the circular reference tube and the investigated elliptical profiles. 36
3.10 Local cut-off-frequency spacing $S(m, e)$ between consecutive EH-polarized Dielectric Modes of the $\nu = 2$ radial family, for the circular reference tube and the investigated elliptical profiles. 37
3.11 Mode-Coupling Loss spectra and squared normalized AFD coefficients $|\widetilde{R}_m|^2$ mapped onto the cut-off frequencies of the corresponding EH-polarized Dielectric Modes. The AFD coefficients, evaluated at $F = 1.6$, are independently rescaled in each panel for visual comparison. The comparison focuses on the MCL falling-edge region. 40
3.12 Boundary spatial wavenumber $k_s = 2\pi m/P$ associated with the azimuthal order of the EH-polarized Dielectric Modes as a function of the normalized cut-off frequency F_c for the circular and elliptical tube geometries. 43
3.13 Squared normalized Fundamental-Mode AFD coefficients $|\widetilde{R}_m|^2$ as a function of the boundary spatial wavenumber $k_s = 2\pi m/P$ for the circular and elliptical tube geometries. Each impulse retains the amplitude of the corresponding Fourier coefficient, while its horizontal position is determined by the spatial wavenumber associated with that harmonic. 44

4.1 Comparison between the original elliptical inner-boundary profiles and the corresponding locally modified geometries in the core-facing region. 49
4.2 Comparison between the curvature distributions of the original elliptical profiles, the corresponding locally modified geometries, and the $b/a = 1.3$ reference ellipse in the core-facing region. 51
4.3 Mode-Coupling Loss spectra of the locally modified tube profiles and of the $b/a = 1.3$ reference ellipse. 53
4.4 Mode-Coupling Loss spectra in the low-frequency falling-edge region for the original elliptical profiles, the corresponding locally modified geometries, and the $b/a = 1.3$ reference ellipse: (a) sharpened $b/a = 1.1$, (b) sharpened $b/a = 1.2$, (c) flattened $b/a = 1.4$, and (d) flattened $b/a = 1.5$. For each comparison, the parent ellipse is shown with a dashed line, whereas the corresponding locally modified profile is shown with a solid line. 55

4.5 Squared normalized AFD coefficients of the Fundamental Mode for the locally modified tube profiles and the $b/a = 1.3$ reference ellipse, evaluated at $F = 1.6$. 56
4.6 Squared normalized AFD coefficients of the Fundamental Mode for the original elliptical profiles, the corresponding locally modified geometries, and the $b/a = 1.3$ reference ellipse, evaluated at $F = 1.6$: (a) sharpened $b/a = 1.1$, (b) sharpened $b/a = 1.2$, (c) flattened $b/a = 1.4$, and (d) flattened $b/a = 1.5$.For each axis ratio, open and filled markers denote the original ellipse and the corresponding locally modified profile, respectively, while black crosses denote the $b/a = 1.3$ reference geometry. 58
4.7 Difference between the normalized cut-off frequencies of the locally modified profiles and those of the corresponding original ellipses, $\Delta F_c = F_c^{\mathrm{mod}} - F_c^{\mathrm{ell}}$, for the EH-polarized Dielectric Modes of the $\nu = 2$ radial family in the azimuthal-order interval, $8 \leq m \leq 25$ 59
4.8 Mode-Coupling Loss spectra and mapped squared normalized AFD coefficients for the original elliptical profiles and the corresponding locally modified geometries. The coefficients are mapped onto the cut-off frequencies of the corresponding EH-polarized Dielectric Modes. Darker tones refer to the original ellipses, while the corresponding lighter tones refer to the locally modified profiles. The AFD distributions are independently rescaled for graphical comparison with the corresponding MCL spectra. 62

List of Tables

3.1 Normalized frequency F_{th} at which the decreasing MCL front crosses the reference level of 10^{-2} dB/km for the circular and elliptical tube geometries. 33
3.2 Cut-off frequencies at $m = 8$ and $m = 25$ and spectral width W for the circular reference tube and the investigated elliptical profiles. . . . 38

4.1 Parameters of the Gaussian deformation applied to the elliptical tube profiles. 49
4.2 Apex curvature of the original elliptical profiles and relative change required to reach the $b/a = 1.3$ reference value. 50

Acronyms

AFD	Azimuthal Fourier Decomposition
AR	Anti-Resonant
CL	Confinement Loss
CLM	Cladding Mode
CM	Core Mode
CMT	Coupled Mode Theory
DM	Dielectric Mode
FCM	Fundamental Core Mode
FM	Fundamental Mode
HC-PCF	Hollow-Core Photonic Crystal Fiber
HLR	High-Loss Region
HM	Hole Mode
IC	Inhibited Coupling
IC-HCPCF	Inhibited-Coupling Hollow-Core Photonic Crystal Fiber
MCL	Mode-Coupling Loss
PBG	Photonic Band Gap
PEC	Perfect Electric Conductor
PML	Perfectly Matched Layer
PMC	Perfect Magnetic Conductor
TB	Transmission Band
TIR	Total Internal Reflection
TLF	Tube Lattice Fiber
TTL	Tube-Tunneling Loss

Abstract

Hollow-core optical fibers have emerged as a promising platform for broadband and low-loss light guidance. Among them, Hollow-Core Inhibited-Coupling Fibers confine light by strongly reducing the interaction between the core mode and the modes supported by the microstructured cladding. In this framework, the geometry of the cladding elements plays a central role in determining the Mode-Coupling Loss (MCL). This thesis theoretically and numerically investigates the effect of cladding-tube shape on MCL in an eight-tube Tube Lattice Fiber, focusing on the azimuthal spectrum of the Fundamental Mode and the cut-off frequencies of the Dielectric Modes. Circular and elliptical tube profiles with different axis ratios are compared. The MCL falling edge exhibits a non-monotonic dependence on tube shape, with the $b/a = 1.3$ geometry providing the largest extension of the low-loss region. The Fundamental-Mode azimuthal content is redistributed with the tube geometry, while the Dielectric-Mode cut-off sequence shifts and compresses. A spatial-wavenumber representation further shows that a substantial part of the cut-off displacement is associated with the global curvilinear scale of the tube boundary. The role of the local core-facing geometry is then isolated by using the $b/a = 1.3$ ellipse as a reference and reshaping the core-facing region of the other elliptical profiles so that their curvature distribution approaches that of the reference, while preserving their overall dimensions. For the modified $b/a = 1.2$, 1.4, and 1.5 profiles, the MCL falling edge moves toward the reference response and the Fundamental-Mode azimuthal spectrum is markedly redistributed, whereas the Dielectric-Mode cut-off frequencies remain nearly unchanged. These results show that the Dielectric-Mode spectral positions are strongly governed by the global boundary scale, whereas the Fundamental-Mode azimuthal content is more sensitive to the detailed shape of the core-facing region. Their combined evolution determines the observed changes in Mode-Coupling Loss.

Chapter 1

Introduction

Hollow-core optical fibers have attracted increasing interest as an alternative to conventional solid-core fibers, since most of the optical power propagates in a gaseous or evacuated region rather than in the dielectric material. The reduced interaction with glass makes it possible to overcome some of the limitations associated with material absorption, Rayleigh scattering, and optical nonlinearities, while enabling broadband transmission and efficient light–gas interaction. Among hollow-core fiber architectures, Inhibited-Coupling fibers guide light by strongly reducing the interaction between the modes propagating in the hollow core and those supported by the microstructured cladding. Tube Lattice Fibers represent one of the simplest configurations based on this mechanism, since their cladding is formed by a single ring of thin dielectric tubes surrounding the hollow core. Their relatively simple structure makes them particularly suitable for investigating the relation between cladding geometry, modal properties, and confinement loss. Recent analyses have shown that Confinement Loss in these fibers can be interpreted in terms of two main contributions: Mode-Coupling Loss, associated with the residual interaction between the Fundamental Mode and the cladding Dielectric Modes, and Tube-Tunneling Loss, associated with direct leakage through the finite cladding structure. The present work focuses on Mode-Coupling Loss and, in particular, on how it is affected by the shape of the cladding tubes. Tube geometry can influence the core–cladding interaction through different mechanisms. A variation of the tube profile can modify the spatial distribution of the Fundamental-Mode field along the dielectric boundary and therefore its azimuthal spectral content. At the same time, it can modify the properties and cut-off frequencies of the Dielectric Modes supported by the tube membrane. Since these two quantities determine, respectively, the relative strength and the approximate spectral position of the interactions contributing to Mode-Coupling Loss, their combined analysis provides a useful framework for investigating tube-shape effects. The aim of this thesis is therefore to theoretically and

numerically investigate the influence of the cladding-tube shape on Mode-Coupling Loss in Hollow-Core Inhibited-Coupling Fibers. An eight-tube Tube Lattice Fiber is considered, combining full-vector numerical simulations with the Azimuthal Fourier Decomposition of the Fundamental Mode and the calculation of the Dielectric-Mode cut-off frequencies through an isolated-tube model. Mode-Coupling Loss is isolated from the tunneling contribution by means of an artificial-index fiber configuration. The analysis first considers the circular tube as a reference and investigates elliptical profiles with increasing axis ratio in order to study the effect of a global variation of the tube shape. In the second part of the thesis, the role of the core-facing region is investigated more directly by locally sharpening or flattening selected elliptical profiles while preserving the global dimensions of the corresponding parent geometry. The comparison between global and local modifications makes it possible to distinguish the influence of different geometrical features of the tube profile on Mode-Coupling Loss.

Chapter 2

Theoretical and Numerical Framework

2.1 Guidance Mechanisms in Optical Fibers

Light guidance in optical fibers can rely on different physical mechanisms. In conventional and hollow-core fibers, the most relevant are Total Internal Reflection (TIR), Photonic Band Gap (PBG) guidance, and Inhibited Coupling (IC).

Conventional solid-core fibers rely on TIR. In a step-index fiber, the refractive index of the core n_{co} is higher than that of the cladding n_{cl}, and guided modes satisfy

$$n_{\mathrm{cl}} < n_{\mathrm{eff}} < n_{\mathrm{co}}. \tag{2.1}$$

Standard silica fibers exhibit minimum attenuation values of the order of 0.2 dB/km around $\lambda = 1550$ nm. At shorter wavelengths, Rayleigh scattering increases, whereas material absorption becomes dominant in the infrared region. Their transmission range is therefore limited by the properties of the material in which light propagates.

In hollow-core fibers, most of the optical power propagates in a gaseous or evacuated region, reducing the interaction with the dielectric material [1]. The refractive index of the guiding region is, however, lower than that of the surrounding dielectric,

$$n_{\mathrm{core}} = n_g < n_d, \tag{2.2}$$

where n_g is the refractive index of the material filling the hollow regions and n_d is that of the dielectric structure. For air-filled fibers, $n_g \simeq 1$. The TIR condition is therefore not satisfied. Hollow-Core Photonic Crystal Fibers (HC-PCF) use a microstructured cladding to confine light in the low-index core. Two relevant guidance mechanisms are Photonic Band Gap guidance and Inhibited Coupling [1]. Their difference can be

described in terms of the modal content of the cladding and its interaction with the Core Modes.

In PBG-HCPCFs, the periodic cladding produces spectral regions in which no cladding state is available with propagation properties compatible with those of the Core Mode. Low-loss guidance is therefore restricted to the spectral range of the photonic band gap [1].

In IC-HCPCFs, instead, Core and Cladding Modes can coexist within the same spectral region. Light confinement does not result from the absence of cladding states, but from the weak interaction between the two modal families [2], [3]. Representative IC structures include Kagome fibers, Tube Lattice Fibers (TLFs), and nested-tube fibers. The same hollow-core structures are also commonly described through the Anti-Resonant (AR) picture. The IC and AR descriptions emphasize different aspects of the confinement mechanism [4]. The AR picture is based on resonant and anti-resonant transmission through the dielectric membranes, whereas the IC description focuses on the interaction between Core and Cladding Modes. In this thesis, the IC description is adopted because the analysis is based on the modal interaction between the Fundamental Core Mode and the modes supported by the cladding.

2.2 Tube Lattice Fiber Structure

Among the different hollow-core fiber architectures based on Inhibited Coupling, the Tube Lattice Fiber (TLF) represents one of the simplest configurations for investigating the relation between the cladding geometry and the optical properties of the fiber [2], [3]. A TLF consists of a single ring of tubular elements surrounding a hollow core and separating it from a homogeneous external jacket. In the conventional configuration, the cladding is composed of N_t circular tubes with inner and outer radii r_{int} and r_{ext}, respectively. The tube-wall thickness is

$$t = r_{\text{ext}} - r_{\text{int}}, \tag{2.3}$$

while δ denotes the gap between adjacent tubes and R_{co} the core radius. The dielectric material forming the tubular elements has refractive index n_d, whereas the hollow core and the tube holes are filled with a lower-index material of refractive index n_g.

Two dimensionless parameters are conveniently introduced to describe the spectral and geometrical properties of the tubular elements: the normalized frequency F and the tube aspect ratio ρ,

$$F = \frac{2t}{\lambda}\sqrt{n_d^2 - n_g^2}, \qquad \rho = \frac{r_{\text{int}}}{r_{\text{ext}}} = 1 - \frac{t}{r_{\text{ext}}}, \tag{2.4}$$

where λ is the free-space wavelength. The normalized frequency F will be used throughout this work to describe the spectral behavior of the fiber, whereas ρ characterizes the relative tube-wall thickness [3], [4].

Figure 2.1 shows a schematic cross-section of the fiber and defines the main geometrical parameters.

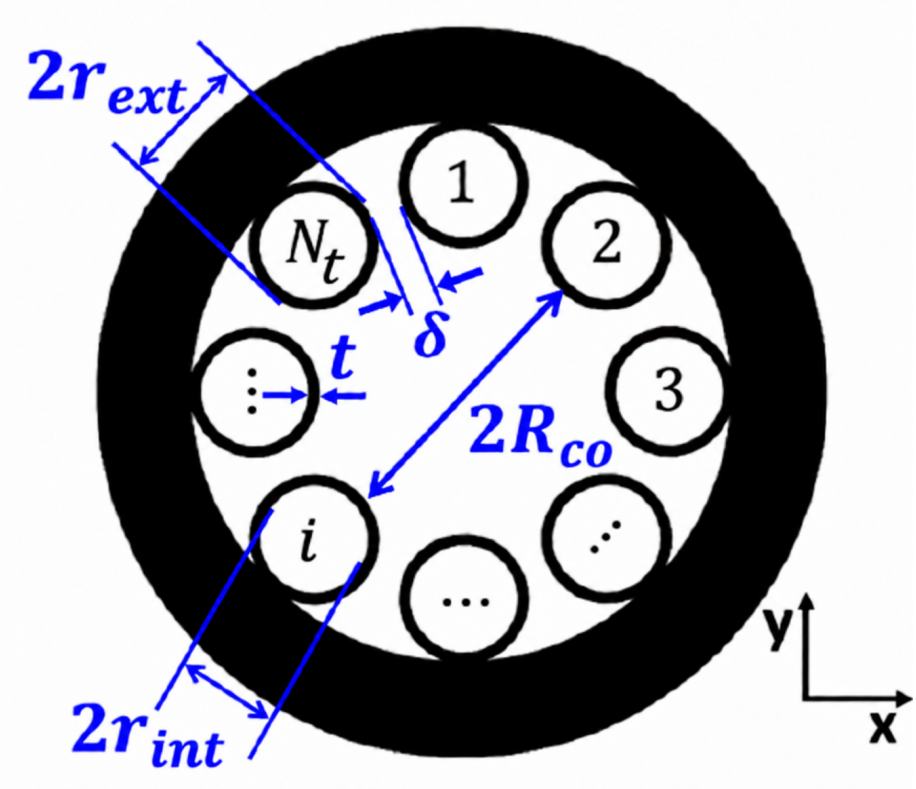


Figure 2.1: Schematic cross-section of a Tube Lattice Fiber and definition of the main geometrical parameters: core radius R_{co}, tube inner and outer radii r_{int} and r_{ext}, tube-wall thickness t, and inter-tube gap δ.

2.3 Modal Structure of the Tube Lattice Fiber

The modal content of a TLF can be divided into three main families: Core Modes (CMs), Hole Modes (HMs), and Dielectric Modes (DMs) [3]. Their representative field distributions and dispersion properties are shown in Fig. 2.2. Core Modes are predominantly localized within the central hollow core, Hole Modes within the hollow regions of the cladding tubes, whereas Dielectric Modes are mainly confined within the dielectric membranes forming the tubular elements. The three modal families exhibit different dispersion properties. In particular, DMs are characterized by comparatively steep dispersion curves, whereas CMs and HMs show a much weaker variation of their effective index with normalized frequency.

The lower panel of Fig. 2.2 shows the corresponding Confinement Loss of the Fundamental Core Mode. The loss spectrum is characterized by an alternation of High-Loss Regions (HLRs) and Transmission Bands (TBs), whose spectral organization will be related below to the modal properties of the tubular elements.

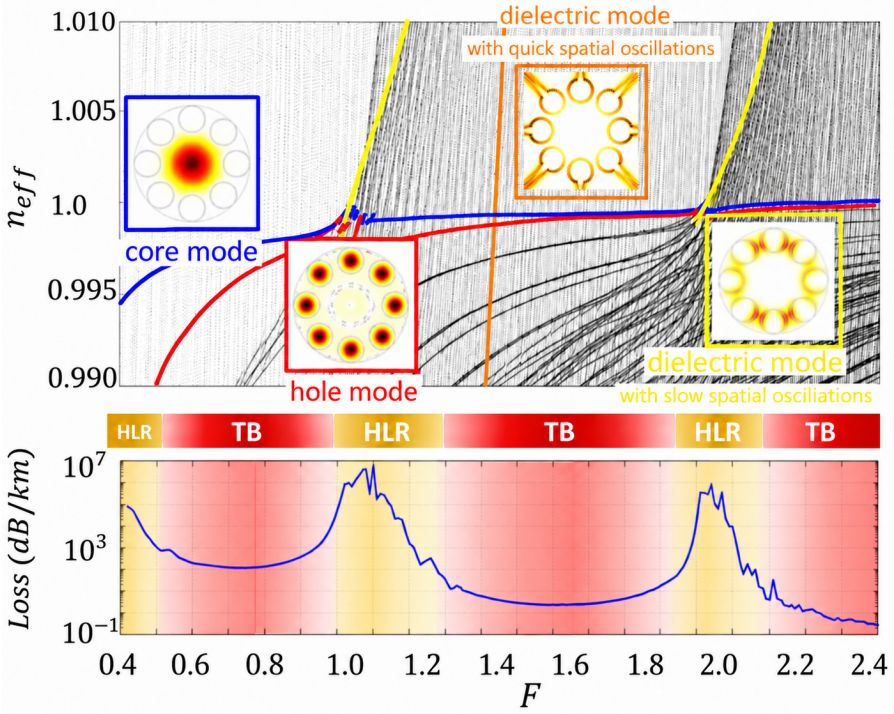


Figure 2.2: Representative modal structure of a Tube Lattice Fiber. The upper panel shows the dispersion curves of the Fundamental Core Mode, a Hole Mode, and representative Dielectric Modes. The lower panel shows the corresponding Confinement Loss of the FCM, with alternating High-Loss Regions and Transmission Bands.

2.3.1 Core Modes

Core Modes are mainly confined within the central hollow region. Their transverse field distributions are similar to the LP modes of a weakly guiding circular waveguide. The lowest-order Core Mode is the $LP_{0,1}$-like Fundamental Core Mode (FCM) [3]. Away from resonant spectral regions, the effective index of the FCM remains close to the refractive index of the low-index material filling the core,

$$n_{\text{eff}}^{\text{FCM}} \simeq n_g, \tag{2.5}$$

and varies only weakly with normalized frequency [3], [5].

2.3.2 Hole Modes

Hole Modes are predominantly confined within the hollow regions of the cladding tubes. Their transverse field distributions resemble those of the modes of a weakly guiding circular waveguide, and they are denoted as $LP_{n,m}^{H}$, where the superscript H distinguishes them from Core Modes. Their dispersion curves vary only weakly with normalized frequency, similarly to those of the Core Modes, as illustrated in Fig. 2.2. In the present work, the analysis is mainly focused on the Dielectric Modes supported by the tube membranes.

2.3.3 Dielectric Modes

Dielectric Modes are mainly localized within the dielectric membranes forming the tubular elements. Each DM is identified by two indices, μ and ν, which describe its azimuthal and radial dependence, respectively. The azimuthal index μ is associated with the number of field oscillations along the tube perimeter, whereas the radial index ν describes the field variation across the tube wall. DMs are further divided into two polarization families, denoted as EH and HE. In EH modes the electric field is mainly oriented along the radial direction, whereas in HE modes it is mainly oriented along the azimuthal direction [3], [4].

As the azimuthal index μ increases, the field distribution exhibits progressively faster oscillations along the tube boundary. This azimuthal structure will become relevant when the interaction between the Fundamental Core Mode and the Dielectric Modes is introduced in Section 2.5.

2.3.4 Single-Tube Approximation and Dielectric-Mode Cut-Off Frequencies

A major simplification in the analysis of the TLF modal structure follows from the geometrical characteristics of its cladding. In the large-pitch regime, the tube-wall thickness is much smaller than the tube diameter,

$$t \ll 2r_{\text{ext}}, \tag{2.6}$$

and the cladding modal structure can be conveniently described through the single-tube approximation [2].

Within this description, the tubular elements are treated as weakly interacting elementary units, and the Cladding Modes of the complete fiber can be related to the modes supported by the individual tubes [3]. Their transverse field distributions and dispersion properties can therefore be approximated by those of an isolated tubular element having the same geometrical and material parameters [3], [6]. The densely populated cladding modal spectrum of the complete TLF can thus be investigated through the much simpler modal problem of a single tube. This approximation is particularly useful for describing the Dielectric Modes and their spectral distribution. Within the isolated-tube model, the cut-off frequency F_c of a Dielectric Mode is defined by the condition

$$n_{\text{eff}}^{\text{DM}}(F_c) = n_g. \tag{2.7}$$

For a fixed radial index ν, the DM with the lowest cut-off frequency is the $\text{HE}_{1,\nu}$ mode, whose cut-off is

$$F_c^{\text{HE}_{1,\nu}} = \nu - 1. \tag{2.8}$$

The remaining modes belonging to the same radial family reach cut-off at progressively reach cut-off at progressively higher normalized frequencies as the azimuthal index increases. For the same pair of indices (μ, ν), EH modes exhibit higher cut-off frequencies than the corresponding HE modes [3], [4].

The DMs can therefore be organized into radial families whose cut-off frequencies are distributed within consecutive normalized-frequency intervals. This spectral organization is reflected in the TLF loss spectrum, where the Transmission Band associated with radial order ν lies within

$$\nu - 1 < F < \nu. \tag{2.9}$$

Within each Transmission Band, modes belonging to the same radial family and

having progressively different azimuthal indices μ reach cut-off at different normalized frequencies. The boundaries between consecutive Transmission Bands occur around integer values of F, corresponding to the High-Loss Regions visible in Fig. 2.2. The distribution of the DM cut-off frequencies depends on the tube geometry and on the dielectric refractive index. Figure 2.3 shows the relation between the azimuthal index μ and the corresponding normalized cut-off frequency F_c for different radial orders and tube aspect ratios ρ.

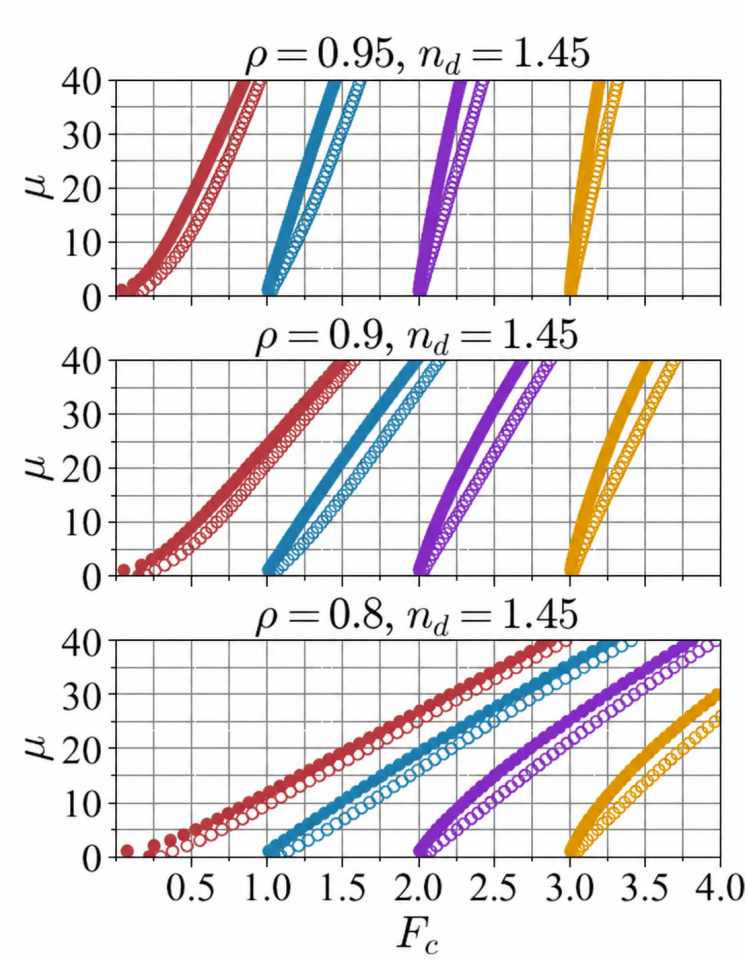


Figure 2.3: Dielectric mode azimuthal index μ and corresponding cut-off frequencies F_c for different values of the radial index ν and tube aspect ratios ρ. Colors indicate the radial order:ν= 1 (red), ν= 2 (blue), ν= 3 (purple), ν= 4 (orange).Empty symbols indicate EH modes and filled symbols indicate HE modes.

For large tube aspect ratios, the DM cut-off frequencies tend to cluster. Increasing ρ makes the μ–F_c curves steeper, so that the variation of F_c with increasing μ becomes smaller [4].

2.4 Confinement Loss: Mode-Coupling Loss and Tube-Tunneling Loss

In hollow-core inhibited-coupling fibers, the Core Modes are intrinsically leaky and therefore exhibit a finite Confinement Loss (CL). The CL is an intrinsic property of the waveguide and is distinct from additional attenuation mechanisms associated, for example, with fabrication imperfections or external perturbations. For a leaky mode, the effective refractive index is complex,

$$n_{\text{eff}} = \text{Re}(n_{\text{eff}}) + j\ \text{Im}(n_{\text{eff}}), \tag{2.10}$$

and the Confinement Loss is obtained from its imaginary part as

$$\text{CL} = 8.686\,\frac{2\pi}{\lambda}\,\left|\text{Im}(n_{\text{eff}})\right|, \tag{2.11}$$

where λ is the free-space wavelength. The result is expressed in dB/m when λ is given in meters. Within each Transmission Band, the Confinement Loss of IC-HCPCFs can be described in terms of two main contributions: Mode-Coupling Loss (MCL) and Tube-Tunneling Loss (TTL) [4]. MCL originates from the residual interaction between the Fundamental Mode and the modes supported by the cladding, mainly Dielectric Modes for the straight fibers considered here. TTL is instead associated with power leakage through the finite tubular structure toward the homogeneous external jacket.

The two mechanisms dominate different spectral regions. On the low-frequency side of a Transmission Band, MCL is the dominant contribution and the loss rapidly decreases with increasing normalized frequency F. At higher frequencies, the loss approaches a flatter region where TTL becomes dominant. The transition between the two regimes is identified by the crossover frequency F_{xo} [4]. The different leakage patterns associated with the two loss regimes can be directly visualized through the radial component of the Poynting vector. Figure 2.4 shows $|\text{Re}(p_r)|$ for a Tube Lattice Fiber at two representative normalized frequencies. At $F = 1.25$, in the MCL-dominated region, the radial power flow is broadly distributed through the cladding tube walls. At $F = 1.66$, corresponding to the TTL-dominated plateau, the power flow becomes concentrated in narrow leakage channels through the tubes toward the external jacket [4].

The Tube-Tunneling Loss can be reduced by introducing additional dielectric layers, which attenuate the evanescent field before it reaches the external jacket. This behavior is illustrated in Fig. 2.5. Increasing the number of nested elements progressively reduces the loss plateau and shifts F_{xo} toward higher normalized frequencies, while

the low-frequency MCL-dominated region remains substantially unchanged [4].

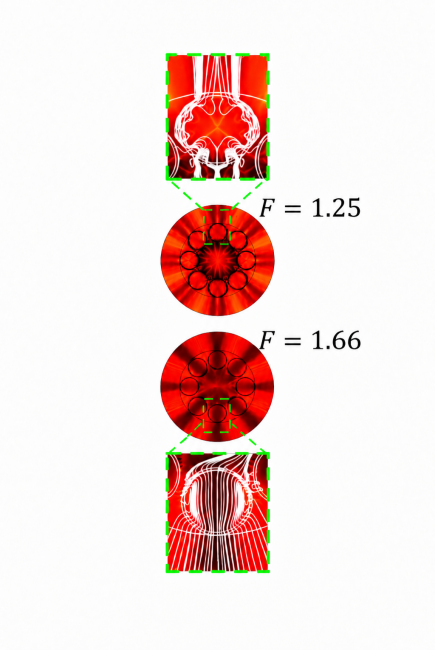
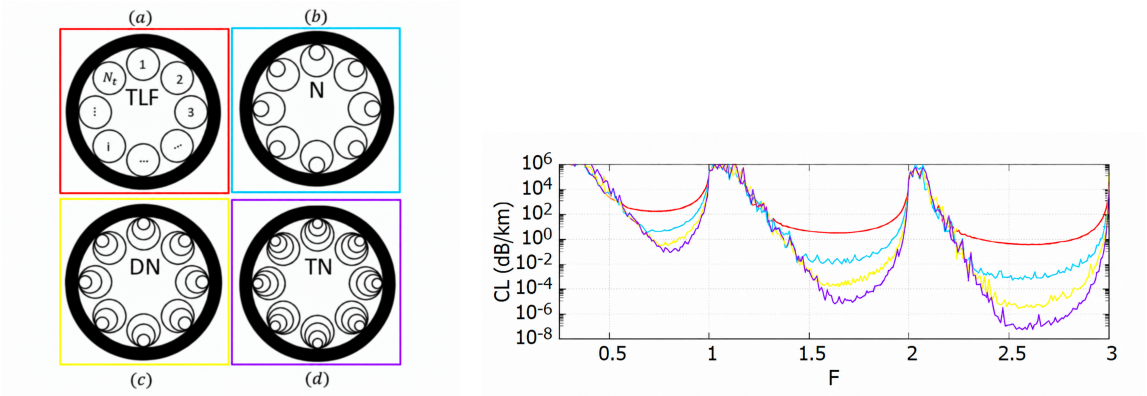


Figure 2.4: Absolute value of the real part of the radial Poynting vector, $|\mathrm{Re}(p_r)|$, for a TLF at $F = 1.25$ and $F = 1.66$. White lines indicate the p_r streamlines.



(a) (b)

Figure 2.5: (a) Cross-sections of Tube Lattice (red), Nested (cyan), Double-Nested (yellow), and Triple-Nested (purple) hollow-core fibers. (b) Confinement-Loss spectra of the corresponding fiber designs shown in (a).

The total Confinement Loss can therefore be approximated as

$$\mathrm{CL}(F) \simeq \mathrm{MCL}(F) + \mathrm{TTL}(F). \tag{2.12}$$

2.5 Inhibited-Coupling Mechanism

The Mode-Coupling Loss introduced in the previous section originates from the residual interaction between the Fundamental Core Mode and the modes supported by the cladding. In IC-HCPCFs, power exchange between a Core Mode (CM) and a Cladding Mode (CLM) requires both longitudinal phase matching and a non-zero transverse field overlap.

The longitudinal phase-matching condition is

$$n_{\text{eff}}^{\text{CM}} = n_{\text{eff}}^{\text{CLM}}, \tag{2.13}$$

while the transverse interaction can be described through the overlap integral

$$K = \iint_{S_\infty} \mathbf{E}_t^{\text{CM}} \cdot \mathbf{E}_t^{\text{CLM}} \, dS, \tag{2.14}$$

where $\mathbf{E}_t^{\text{CM}}$ and $\mathbf{E}_t^{\text{CLM}}$ are the transverse electric-field components of the two modes.

The Fundamental Core Mode has a slowly varying transverse field, whereas Cladding Modes can exhibit much faster spatial oscillations. For CLMs with a rapidly oscillating transverse field, positive and negative contributions to the overlap integral tend to compensate, giving

$$K \simeq 0. \tag{2.15}$$

The coupling with the FCM is consequently weak. CLMs with slower spatial oscillations exhibit a larger overlap and can interact more strongly with the Core Mode [3], [7]. Both Core and Cladding Modes are leaky and are therefore not strictly orthogonal. Their complex propagation constants can be written as

$$\gamma_{\text{CM}} = \beta_{\text{CM}} - j\alpha_{\text{CM}}, \qquad \gamma_{\text{CLM}} = \beta_{\text{CLM}} - j\alpha_{\text{CLM}}, \tag{2.16}$$

where β is the phase constant and α the attenuation coefficient. Their interaction can be described through Coupled Mode Theory (CMT) [3]. The propagation-constant detuning is defined as

$$\Delta\beta = \beta_{\text{CLM}} - \beta_{\text{CM}} = \frac{2\pi}{\lambda}\left(n_{\text{eff}}^{\text{CLM}} - n_{\text{eff}}^{\text{CM}}\right), \tag{2.17}$$

and the differential attenuation as

$$\Delta\alpha = \alpha_{\text{CLM}} - \alpha_{\text{CM}}. \tag{2.18}$$

The propagation constants of the coupled system are then given by [3]

$$\gamma_{\pm} = \frac{\gamma_{\mathrm{CM}} + \gamma_{\mathrm{CLM}}}{2} \pm \sqrt{\left(\frac{\gamma_{\mathrm{CLM}} - \gamma_{\mathrm{CM}}}{2}\right)^2 + \kappa^2}, \tag{2.19}$$

where κ is the coupling coefficient between the two modes. While K describes the transverse field overlap, κ is the coupling coefficient entering the CMT model.

At phase matching, $\Delta\beta = 0$, two different coupling regimes are obtained depending on the relative values of κ and $\Delta\alpha$. In the weak-coupling regime,

$$2|\kappa| < \Delta\alpha, \tag{2.20}$$

the dispersion curves cross, whereas the attenuation curves exhibit an anti-crossing. In the strong-coupling regime,

$$2|\kappa| > \Delta\alpha, \tag{2.21}$$

the dispersion curves exhibit an anti-crossing, while the attenuation curves cross [3]. The two cases are shown in Fig. 2.6.

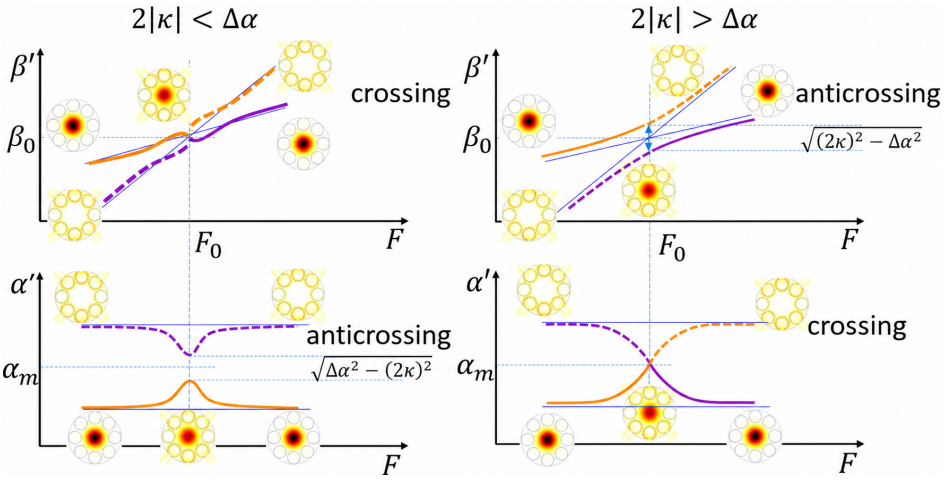


Figure 2.6: Dispersion and attenuation curves in the weak- and strong-coupling regimes. In weak coupling the dispersion curves cross while the attenuation curves exhibit an anti-crossing; in strong coupling the opposite behavior occurs.

In the limit of very weak coupling,

$$2|\kappa| \ll \Delta\alpha, \tag{2.22}$$

the attenuation of the Core Mode at phase matching can be approximated as

$$\alpha_{\mathrm{CM}} \simeq \alpha_{\mathrm{CM},0} + \frac{|\kappa|^2}{\Delta\alpha}, \tag{2.23}$$

where $\alpha_{\mathrm{CM},0}$ is the attenuation of the Core Mode in the absence of coupling. The loss enhancement associated with the interaction therefore scales quadratically with

the coupling coefficient in this limit.

In a Tube Lattice Fiber, the single-tube description introduced in Section 2.3.4 also provides a useful interpretation of the transverse overlap. Since a Cladding Mode of the complete fiber can be expressed in terms of the contributions associated with the individual tubular elements, the total overlap can be written as

$$K = \sum_{i=1}^{N_t} K_i = \sum_{i=1}^{N_t} \iint_{S_{\mathrm{tube},i}} \mathbf{E}_t^{\mathrm{CM}} \cdot \mathbf{E}_{t,i}^{\mathrm{CLM}} \, dS, \tag{2.24}$$

where $\mathbf{E}_t^{\mathrm{CM}}$ is the transverse electric field of the Core Mode, $\mathbf{E}_{t,i}^{\mathrm{CLM}}$ is the contribution of the Cladding Mode associated with the i-th tube, and $S_{\mathrm{tube},i}$ is the corresponding integration region [8].

The global core–cladding interaction can therefore be interpreted as the sum of the contributions associated with the individual tubular elements. For the Fundamental Core Mode considered here, $n_{\mathrm{eff}}^{\mathrm{FCM}} \simeq n_g$, as expressed in Eq. 2.5. Therefore, the longitudinal phase-matching condition with a Dielectric Mode,

$$n_{\mathrm{eff}}^{\mathrm{FCM}} = n_{\mathrm{eff}}^{\mathrm{DM}}, \tag{2.25}$$

is approximately fulfilled when

$$n_{\mathrm{eff}}^{\mathrm{DM}} \simeq n_g. \tag{2.26}$$

According to the cut-off condition introduced in Section 2.3.4, the corresponding phase-matching frequency can therefore be approximated by the Dielectric-Mode cut-off frequency,

$$F_{\mathrm{PM}}^{\mu,\nu} \simeq F_c^{\mu,\nu}. \tag{2.27}$$

The transverse overlap is strongly influenced by the azimuthal structure of the Dielectric Modes. As the azimuthal index μ increases, the DM field oscillates more rapidly along the tube perimeter, producing a stronger cancellation in the overlap with the slowly varying Fundamental Core Mode.

This behavior is quantitatively illustrated in [3], where the coupling coefficient decreases from $|\kappa| = 610$ m^{-1} for the $\mathrm{EH}_{3,3}$ mode to $|\kappa| = 285$ m^{-1} for $\mathrm{EH}_{4,3}$, and further to $|\kappa| = 16$ m^{-1} for $\mathrm{EH}_{8,3}$. Dielectric Modes characterized by larger azimuthal indices therefore interact progressively more weakly with the Fundamental Core Mode. The combined evolution of the DM cut-off frequencies and of their azimuthal order provides an interpretation of the alternating High-Loss Regions and Transmission Bands introduced in Section 2.3. Around integer values of F, the FCM can interact with DMs characterized by relatively low azimuthal indices and slower

spatial oscillations, resulting in stronger core–cladding interaction and higher loss. Moving away from the integer values of F, the DMs reaching cut-off are characterized by progressively larger azimuthal indices. Their faster spatial oscillations reduce the transverse overlap with the FCM, and the corresponding interaction becomes progressively weaker [3]. The spectral evolution of Mode-Coupling Loss is therefore determined by two complementary properties: the DM cut-off frequencies, which identify the approximate spectral positions of the possible interactions, and the transverse matching between the Fundamental Core Mode and the corresponding Dielectric Modes.

2.6 Azimuthal Fourier Decomposition

The Inhibited-Coupling description introduced in the previous section shows that the interaction between the Fundamental Core Mode and the Dielectric Modes depends on their transverse field overlap. In general, this overlap depends on the spatial distributions of both modes. In a conventional TLF with circular tubes, however, the azimuthal dependence of a Dielectric Mode of order μ is approximately sinusoidal and is therefore associated with a single azimuthal order, represented by the two symmetric Fourier components $m = \pm\mu$ [4], [7].

As a consequence, the azimuthal overlap with a given Dielectric Mode selects the Fundamental-Mode Fourier component having the corresponding azimuthal order. The relative transverse matching with DMs of different orders can therefore be investigated by considering the azimuthal Fourier content of the Fundamental Mode. The Azimuthal Fourier Decomposition (AFD) provides a convenient tool for this purpose.

For a circular tube, a local polar coordinate system (r, θ) is introduced with its origin at the tube center. The transverse electric field of the Fundamental Mode is sampled along the inner dielectric boundary,

$$r = r_{\text{int}}, \tag{2.28}$$

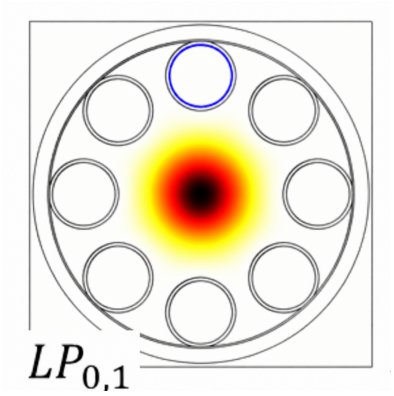
and expressed as a function of the azimuthal coordinate θ. The inner boundary is considered because the Fundamental-Mode field amplitude, and consequently its contribution to the core–cladding overlap, is larger there than at the outer tube boundary [7]. The corresponding AFD coefficients are defined as

$$R_m = \frac{1}{2\pi} \int_0^{2\pi} E_t(\theta) e^{-jm\theta}\, d\theta, \tag{2.29}$$

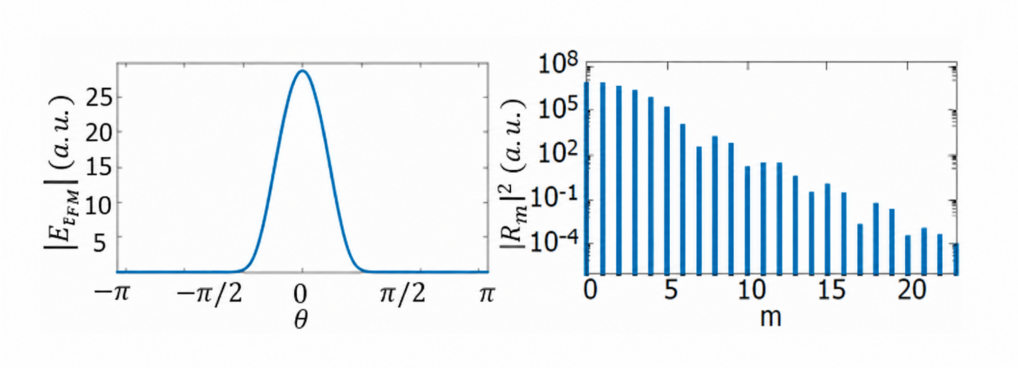
where m is the azimuthal Fourier order and $E_t(\theta)$ denotes the transverse electric field

of the Fundamental Mode sampled along the inner tube boundary [4], [7].

A representative example is shown in Fig. 2.7. The Fundamental-Mode field is localized around the portion of the tube boundary facing the hollow core and rapidly decreases away from this region. Its Fourier spectrum is consequently characterized by coefficients whose magnitude decreases with increasing azimuthal order.



(a)



(b)

Figure 2.7: Azimuthal Fourier Decomposition of the Fundamental Core Mode. (a) FCM field distribution in the TLF cross-section, with the inner boundary of the selected tube highlighted in blue. (b) Transverse electric field sampled along this boundary and corresponding squared AFD coefficients $|R_m|^2$.

For an ideal circular tube, a Dielectric Mode with azimuthal index μ has its dominant Fourier components at $m = \pm\mu$. Owing to the orthogonality of the azimuthal harmonics, the overlap with the Fundamental Mode selects the Fundamental-Mode Fourier component having the corresponding azimuthal order. Restricting the representation to non-negative Fourier orders, as adopted throughout this work, the azimuthal selection rule can therefore be written as

$$m = \mu. \tag{2.30}$$

The coefficient R_μ consequently quantifies the Fundamental-Mode azimuthal

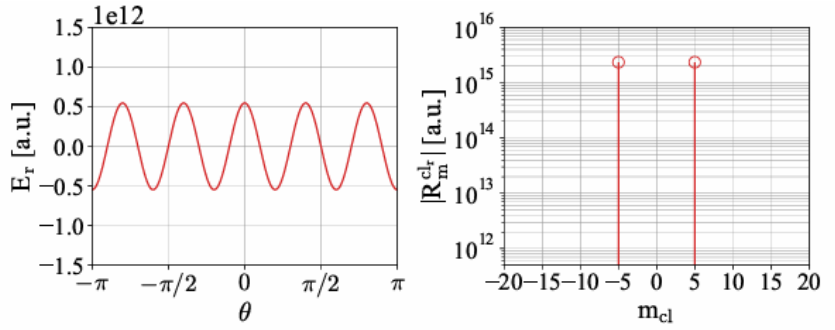


Figure 2.8: Azimuthal field profile and corresponding Fourier spectrum of the $EH_{5,3}$ Dielectric Mode. The approximately sinusoidal field distribution gives rise to dominant Fourier components at $m = \pm 5$, corresponding to the azimuthal mode order $\mu = 5$.

component available for interaction with a Dielectric Mode of order μ. Since the magnitude of R_m decreases rapidly with increasing m, DMs of larger azimuthal order overlap with progressively weaker Fundamental-Mode components. The azimuthal matching between the Fundamental Mode and a Dielectric Mode can be quantified through the Azimuthal Spectra Overlap (ASO), denoted by g. Within the single-tube approximation, the ASO provides a Fourier-domain representation of the transverse modal overlap and is therefore related to the overlap integral K introduced in Section 2.5,

$$K_{\mu,\nu} \propto g_{\mu,\nu}(r_{\text{int}}). \tag{2.31}$$

For a circular tube, since the Fourier spectrum of a Dielectric Mode of azimuthal order μ is concentrated at $m = \pm\mu$, the ASO is mainly determined by the Fundamental-Mode Fourier component of the corresponding order, R_μ. This relation is summarized in Fig. 2.9, which connects the Fundamental-Mode azimuthal spectrum, the Dielectric-Mode cut-off distribution, and the corresponding squared Azimuthal Spectra Overlap.

In the very weak-coupling regime and within a given radial family, the relative loss contribution associated with a Dielectric Mode of indices (μ, ν) can therefore be related to the corresponding squared AFD coefficient as

$$\delta\alpha_{\mu,\nu} \propto |R_\mu|^2. \tag{2.32}$$

The proportionality factor depends on the fiber geometry, so that $|R_\mu|^2$ describes the relative strength of the different modal contributions rather than their absolute loss [4]. The AFD coefficients therefore provide information on the relative strength of the individual coupling contributions, whereas their spectral positions are determined by the Dielectric-Mode dispersion. As discussed in Section 2.5, the phase-matching frequency between the Fundamental Core Mode and a Dielectric

Mode is well approximated by the corresponding cut-off frequency,

$$F_{\mathrm{PM}}^{\mu,\nu} \simeq F_{c}^{\mu,\nu}. \tag{2.33}$$

The Mode-Coupling Loss within a Transmission Band can therefore be interpreted as the superposition of contributions associated with the Dielectric Modes belonging to the corresponding radial family. Each contribution is located close to the cut-off frequency $F_c^{\mu,\nu}$, while its relative strength is related to $|R_\mu|^2$ [4], [7].

The spectral behavior of MCL is consequently determined by two complementary quantities: the Dielectric-Mode cut-off frequencies, which identify the approximate spectral positions of the core–cladding interactions, and the azimuthal Fourier content of the Fundamental Mode, which describes their relative strength.

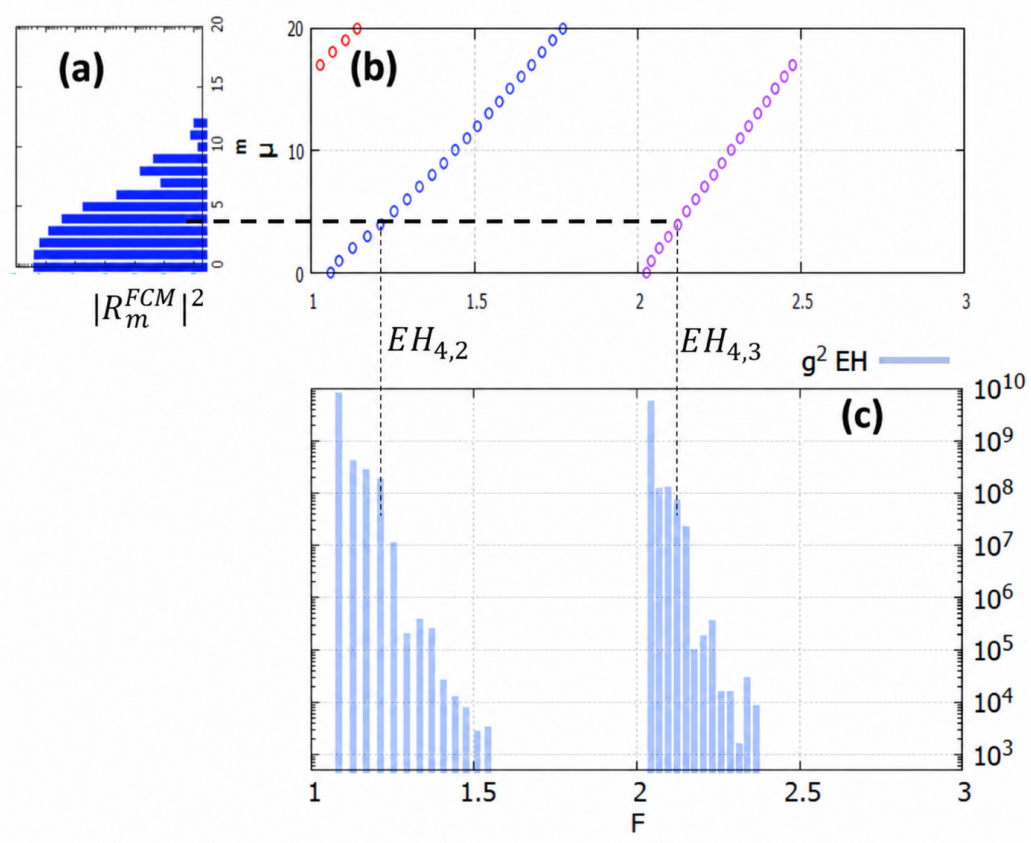


Figure 2.9: Relation between the FCM azimuthal spectrum, the Dielectric-Mode cut-off frequencies, and the corresponding coupling contributions. (a) Squared FCM AFD coefficients $|R_m^{\mathrm{FCM}}|^2$. (b) Cut-off frequencies of EH modes with radial orders $\nu = 2$ and $\nu = 3$. (c) Corresponding squared Azimuthal Spectra Overlap g_{EH}^2. The dashed lines highlight the case $\mu = 4$.

2.7 Artificial-Index Fiber for MCL Isolation

The theoretical framework introduced in the previous sections describes Mode-Coupling Loss as one of the two contributions to the total Confinement Loss. In a direct numerical simulation of the real fiber, however, MCL and Tube-Tunneling Loss are simultaneously included. To isolate the MCL contribution, an artificial-fiber configuration is therefore introduced in which the tunneling channels are suppressed while the core–cladding modal interaction is preserved [4]. The geometry of the original TLF is retained and a third material with refractive index n_a is introduced. Its refractive index satisfies

$$n_a < n_{\text{eff}}^{\text{FM}} < n_g, \tag{2.34}$$

where $n_{\text{eff}}^{\text{FM}}$ is the effective index of the Fundamental Mode and n_g is the refractive index of the material filling the hollow regions [4]. Since $n_a < n_{\text{eff}}^{\text{FM}}$, the field becomes strongly evanescent inside the artificial regions, suppressing the direct tunneling paths toward the external jacket. At the same time, the ""artificial material"" is kept at a finite distance from the dielectric membranes in order to preserve the modal properties of the Fundamental Mode and of the Dielectric Modes, and therefore their mutual interaction.

The "artificial-index" configuration adopted in this work is shown in Fig. 2.10. The "artificial material" is introduced inside the tube holes and in the inter-tube regions surrounding the cladding elements.

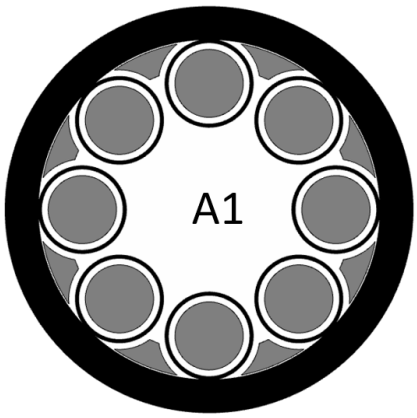


Figure 2.10: Artificial-index TLF configuration used to isolate Mode-Coupling Loss. The artificial low-index material is introduced inside the tube holes and in the inter-tube regions and is kept at a finite distance from the dielectric tube walls in order to preserve the original modal structure.

In the numerical implementation reported in [4], the artificial refractive index is set to

$$n_a = 0.9\, n_g, \tag{2.35}$$

and the minimum distance between the "artificial material" and the dielectric tube walls is

$$d_a = 2t. \tag{2.36}$$

For hollow-core fibers with $n_g \simeq 1$, the condition in Eq. 2.34 requires $n_a < 1$. The artificial medium is therefore a numerical construct introduced to suppress tunneling rather than a physical material. The effect of the "artificial material" on the modal properties was verified in [4]. The variation of the Fundamental-Mode Field Diameter remains below approximately 1.5%, while the change in effective index is below 2×10^{-5}. The Dielectric-Mode structure is also substantially preserved, with only small deviations in the high-loss spectral regions.

The loss calculated with this "artificial-index" configuration can therefore be attributed, to a very good approximation, to Mode-Coupling Loss,

$$\mathrm{CL_{A1}} \simeq \mathrm{MCL}. \tag{2.37}$$

This behavior is illustrated in Fig. 2.11, where the Confinement Loss of the original TLF is compared with that of the corresponding "artificial-index" configuration A1. The two curves are nearly coincident in the MCL-dominated region, whereas they progressively separate in the Tube-Tunneling-dominated region.

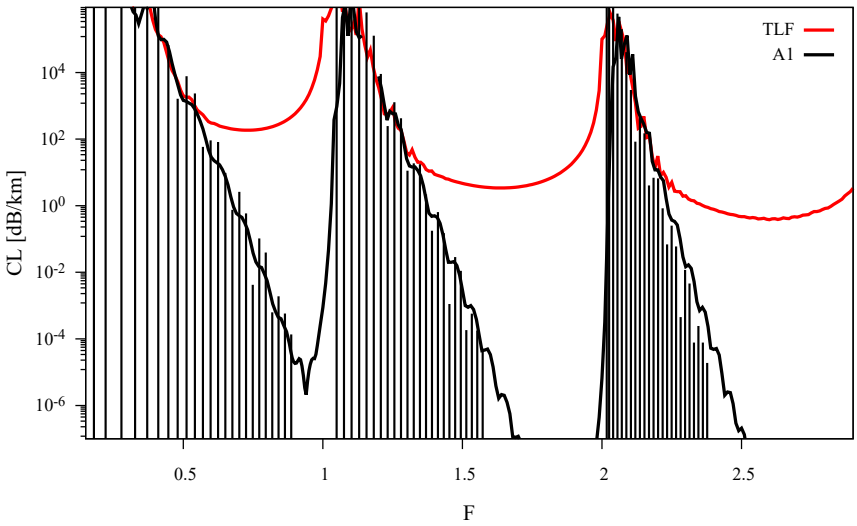


Figure 2.11: Comparison between the Confinement Loss of the original TLF and that of the corresponding "artificial-index" configuration A1. The vertical bars represent the squared Fundamental-Mode AFD coefficients $|R_m|^2$ positioned at the cut-off frequencies of the corresponding Dielectric Modes.

Chapter 3

Effect of Elliptical Tube Geometry

Tube geometry plays a relevant role in determining the mode-coupling contribution to the confinement loss of Hollow-Core Inhibited-Coupling Fibers. A modification of the cladding tube shape can affect the modal properties involved in the coupling between the Fundamental Mode (FM) and the Dielectric Modes (DMs). In particular, changes in the tube geometry can modify both the azimuthal spectrum of the FM along the tube boundary and the spectral distribution of the DM cut-off frequencies, thus affecting the Mode-Coupling Loss (MCL). In this chapter, the impact of tube shape is investigated by taking the conventional circular tube as the reference configuration and considering elliptical cladding tubes with different axis ratios. The resulting confinement-loss spectra are analyzed together with the evolution of the FM azimuthal spectrum and of the DM cut-off frequencies, with the aim of understanding how ellipticity modifies the core–cladding coupling mechanism and the transmission properties of the fiber.

3.1 Reference and Elliptical Tube Geometries

Starting from the circular reference configuration, a set of elliptical tube geometries with semi-minor axis a, kept fixed at $9.45\,\mu$m, and semi-major axis b is considered. The ellipticity is defined as the axis ratio

$$e = \frac{b}{a}, \tag{3.1}$$

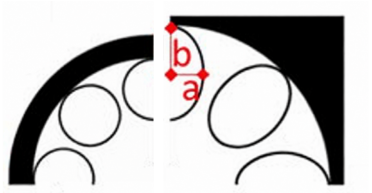
In the local coordinate system used to define a single tube, the elliptical inner boundary is parameterized as

$$x = a\sin\theta, \qquad y = -b\cos\theta, \tag{3.2}$$

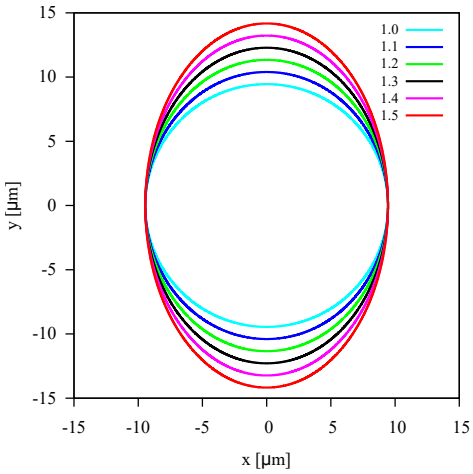
where θ is the angular parameter. The outer dielectric boundary is obtained by offsetting the inner profile by a constant distance th along the local normal direction, so that the tube-wall thickness is preserved along the entire contour. Five elliptical configurations are considered, corresponding to

$$e = 1.1,\ 1.2,\ 1.3,\ 1.4,\ 1.5, \tag{3.3}$$

while $e = 1$ identifies the circular reference case.



(a)



(b)

Figure 3.1: (a) Cross sections of TLF with circular and elliptical tubes. (b) Inner-boundary profiles for different tube axis ratios e.

3.2 Numerical Model

The tube profiles defined in the previous section are used as cladding elements of an eight-tube Tube Lattice Fiber. The complete fiber geometry consists of eight identical tubular elements arranged around a hollow core of radius

$$R_{\mathrm{co}} = 18.75\,\mu\mathrm{m}. \tag{3.4}$$

The tube-wall thickness is fixed at

$$th = 0.55\,\mu\mathrm{m}, \tag{3.5}$$

while the tube-to-tube gap is kept constant for all the investigated configurations. The same tube profile is used for all eight cladding elements and is rotated according to its angular position around the hollow core. For the Mode-Coupling-Loss calculations, the complete-fiber model is implemented using the A1 artificial-index configuration introduced in Section 2.7, so the artificial low-index material is introduced inside the tube holes and in the inter-tube regions.

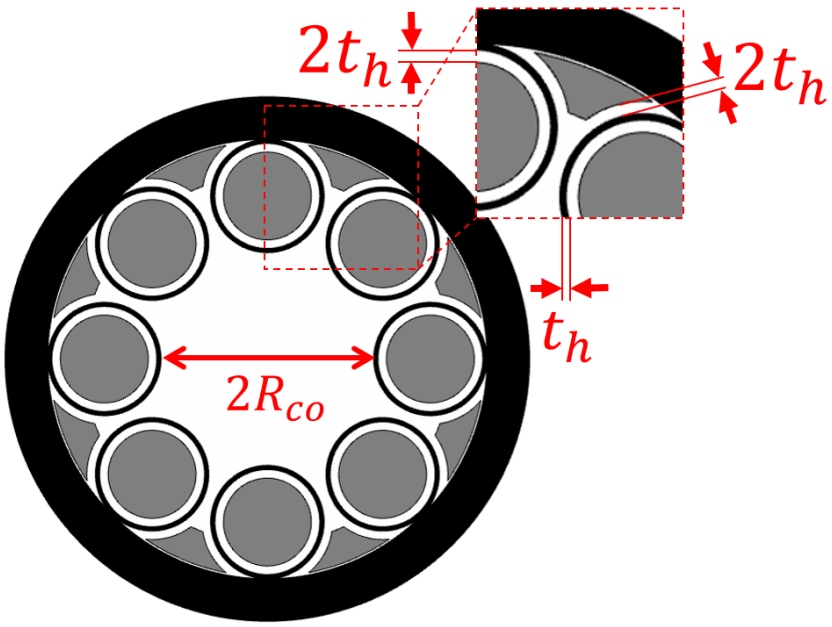


Figure 3.2: Cross-section of the eight-tube TLF used in the numerical analysis, showing the main geometrical parameters and the artificial-index regions employed in the A1 configuration.

The resulting fiber configurations are investigated by means of full-vector finite-element modal simulations performed with COMSOL Multiphysics. MATLAB is used for the generation of the different tube profiles, the execution of the numerical sweeps, and the post-processing of the simulated modal fields.

Two complementary numerical models are employed. The first one describes the complete fiber and provides the FCM field distribution and the corresponding loss. The second one considers an isolated tubular element and is used to determine the properties and cut-off frequencies of the Dielectric Modes according to the single-tube approximation. The dielectric tubes are modeled with refractive index $n_d = 1.45$, while the hollow core and the remaining gas regions have refractive index $n_g = 1$. To provide a consistent comparison among the different fiber configurations, the numerical analyses are carried out using the same geometrical, material, and numerical parameters, except for the tube geometry intentionally varied in each investigation. The differences observed in the MCL spectra, in the AFD coefficients, and in the Dielectric-Mode properties can therefore be directly related to the considered geometrical modification.

Unless otherwise specified, the analysis is performed in the normalized-frequency interval $1 < F < 2$, corresponding to the Transmission Band between the High-Loss Regions located around $F = 1$ and $F = 2$. This interval is used as a common spectral range for the comparison of all the investigated geometries [3], [4]. For the complete-fiber calculations, the eigenvalue problem is solved through the *Electromagnetic Waves* interface and a Mode Analysis study. Owing to the two orthogonal symmetry planes of the structure, only one quarter of the complete fiber cross-section is simulated. A PMC condition is imposed on the vertical symmetry boundary, whereas a PEC condition is applied to the horizontal one. The outer boundary is terminated by Perfectly Matched Layers (PMLs), as commonly adopted in the finite-element analysis of TLF leaky modes [2], [9]. For the artificial-index configuration used throughout this work, the calculated loss can therefore be interpreted as

$$MCL \simeq CL. \tag{3.6}$$

The Confinement Loss is evaluated from the imaginary part of the complex effective index according to Eq. 2.11.

For the non-circular tube profiles, quantities evaluated along the tube boundary are parameterized through the curvilinear coordinate s, defined as the arc length along the considered contour. For a complete inner boundary of perimeter P, the normalized curvilinear coordinate and the corresponding angular coordinate are defined as

$$s_{\mathrm{norm}} = \frac{s}{P}, \qquad \phi = \frac{2\pi s}{P} = 2\pi s_{\mathrm{norm}}. \tag{3.7}$$

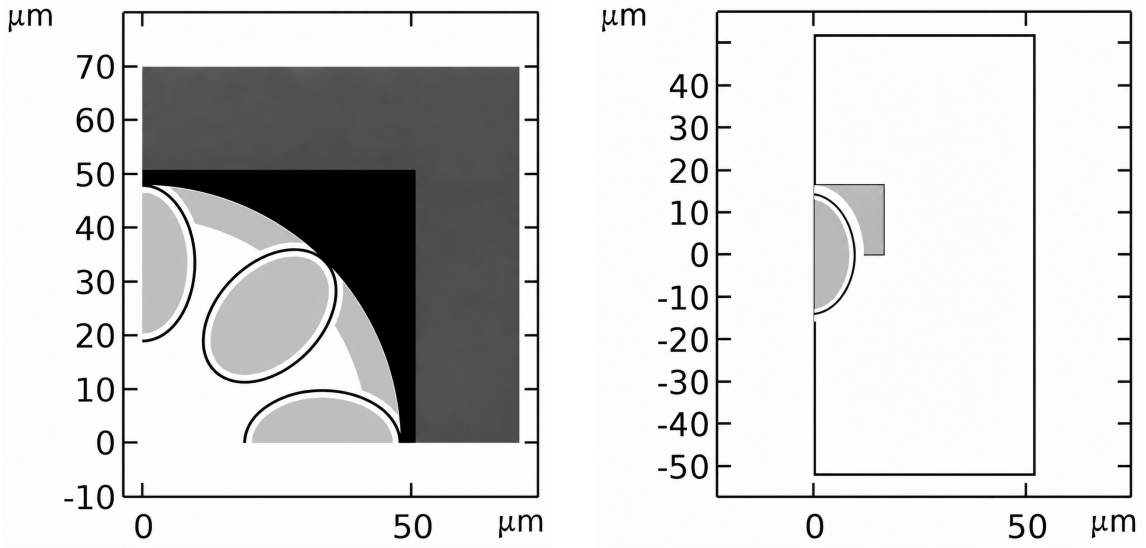
The Fundamental-Mode field obtained from the complete-fiber calculation is also used for the Azimuthal Fourier Decomposition introduced in Section 2.6. Following the

AFD approach, the field is sampled along the inner boundary of one cladding tube [4], [7]. For the AFD-based comparison developed in the following sections, attention is focused on the EH-polarized Dielectric-Mode family. The transverse overlap between the Fundamental Mode and a Dielectric Mode contains contributions from both the normal and tangential field components. For EH modes, however, the tangential component at the tube boundary is negligible with respect to the normal one. Their coupling with the Fundamental Mode is therefore mainly determined by the overlap between the corresponding normal field components. Accordingly, the AFD of the Fundamental Mode is evaluated from the local normal component of its transverse electric field. Denoting by $\mathbf{n} = (n_x, n_y)$ the local unit normal vector to the inner tube boundary, the considered field component is

$$E_n^{\mathrm{FCM}} = \mathbf{E}_t^{\mathrm{FCM}} \cdot \mathbf{n} = E_x^{\mathrm{FCM}} n_x + E_y^{\mathrm{FCM}} n_y. \tag{3.8}$$

This local definition provides the natural extension of the radial field component used for circular tubes to the non-circular profiles considered in this work. The AFD coefficients are then evaluated as a function of the curvilinear angular coordinate ϕ.

A separate numerical model is employed to determine the Dielectric-Mode cut-off frequencies. In accordance with the single-tube approximation discussed in Section 2.3, the complete cladding is replaced by an isolated tubular element having the same wall thickness, material properties, and boundary profile as the corresponding cladding tube [2], [3].



(a) Complete-fiber model. (b) Isolated-tube model.

Figure 3.3: Computational domains employed in the numerical analysis: (a) quarter cross-section of the complete fiber used for the Fundamental-Mode and loss calculations; (b) half cross-section of the isolated tubular element used for the calculation of the Dielectric-Mode cut-off frequencies.

The isolated-tube calculation is performed using the *Electromagnetic Waves, Frequency Domain* interface together with a Mode Analysis study. The computational domain is reduced to one half of the tube cross-section. At each frequency in the considered normalized-frequency interval, 20 eigenmodes are searched in the vicinity of the air line, with the eigenvalue search centred at $n_{\text{eff}} = 1.0002$. The frequency step is $\Delta F = 10^{-3}$. The tube modes are identified from the fraction of the modal field localized in the dielectric wall. The selected modes are then separated into the HE and EH polarization families. As discussed in Section 2.3.3, HE modes are characterized by a predominantly tangential electric field, whereas the electric field of EH modes is mainly normal to the tube boundary [3], [4]. Modes for which neither polarization is sufficiently dominant are excluded from the subsequent classification.

The azimuthal order m is determined from the electric-field variation along a curve located at half of the dielectric-wall thickness. Since only one half of the tube boundary is considered in the isolated-tube model, the curvilinear coordinate introduced above is mapped into $\phi = \frac{\pi s}{L}$, where L is the length of the sampled half-boundary. The eigenfields returned by the numerical solver are complex and defined up to an arbitrary global phase. The azimuthal-order estimation is therefore performed on the field modulus, avoiding any dependence on the phase selected by the eigensolver. The numerical profiles are fitted to

$$\begin{cases} |E_\tau(\phi)| \simeq A_m |\sin(m\phi)|, & \text{HE}, \\ |E_n(\phi)| \simeq A_m |\cos(m\phi)|, & \text{EH}, \end{cases} \tag{3.9}$$

The integer providing the best least-squares agreement is assigned as the azimuthal order m of the mode.

The radial index ν is determined independently by sampling the numerical quantity $H_z + E_z$ along several lines locally normal to the dielectric wall. Since the eigenfields are complex and defined up to an arbitrary global phase, two orthogonal real projections are compared and the one providing the strongest overall modal amplitude is selected and used consistently for the entire mode. Sampling lines characterized by a negligible field amplitude are discarded.

For each valid line, the radial index is obtained from the number of sign changes across the dielectric wall,

$$\nu = N_{\text{sc}} + 1, \tag{3.10}$$

where N_{sc} is the number of sign changes. The final value of ν is taken as the value occurring most frequently among the valid sampling lines.

The procedure provides the azimuthal and radial orders (m, ν) used to identify

and follow the Dielectric Modes throughout the frequency sweep. For each classified modal branch, the real part of the effective index is finally followed as a function of F. According to the cut-off condition introduced in Section 2.3.4,

$$\mathrm{Re}\left[n_{\mathrm{eff}}^{\mathrm{DM}}(F_c)\right] = n_g, \tag{3.11}$$

which reduces to $\mathrm{Re}[n_{\mathrm{eff}}^{\mathrm{DM}}(F_c)] = 1$ for the air-filled structures considered here. When the air-line crossing occurs between two consecutive simulated frequencies, the corresponding cut-off frequency is obtained by linear interpolation.

The complete-fiber and isolated-tube calculations therefore provide the two quantities required for the subsequent interpretation of Mode-Coupling Loss: the azimuthal spectrum of the Fundamental Mode and the spectral distribution of the Dielectric-Mode cut-off frequencies.

3.3 Inner-Boundary Curvature Analysis

To characterize the geometrical changes introduced by the elliptical deformation, the curvature of the inner tube boundary is considered. For the circular reference tube, the curvature is constant along the entire boundary, whereas for an elliptical tube it depends on the position along the profile. For the elliptical parametrization introduced in Section 3.1, the curvature is given by

$$\kappa(\theta) = \frac{ab}{\left(a^2\cos^2\theta + b^2\sin^2\theta\right)^{3/2}}. \tag{3.12}$$

In the circular case, $a = b$, and Eq. (3.12) reduces to

$$\kappa_{\mathrm{circ}} = \frac{1}{a}, \tag{3.13}$$

which, for $a = 9.45\,\mu\mathrm{m}$, gives

$$\kappa_{\mathrm{circ}} \simeq 1.06 \times 10^5\,\mathrm{m}^{-1}. \tag{3.14}$$

For the elliptical geometries, the maximum curvature is reached at the ends of the major axis. The point of the inner tube boundary directly facing the hollow core is hereafter referred to as the core-facing tube apex. At this point,

$$\kappa_{\mathrm{apex}} = \frac{b}{a^2}, \tag{3.15}$$

while at the ends of the minor axis the curvature is

$$\kappa_{\mathrm{lat}} = \frac{a}{b^2}. \tag{3.16}$$

Since $b = ea$, the two values can be rewritten as

$$\kappa_{\mathrm{apex}} = \frac{e}{a}, \qquad \kappa_{\mathrm{lat}} = \frac{1}{e^2 a}. \tag{3.17}$$

Therefore, keeping the semi-minor axis a constant, an increase of the axis ratio produces an increase of the curvature at the core-facing apex and a simultaneous decrease of the curvature in the lateral regions.

Figure 3.4 shows the curvature distribution along the inner tube boundary for the circular reference tube and for the elliptical configurations. The curvature is represented as a function of the normalized arc-length coordinate s_{norm} introduced in 3.2, with the core-facing tube apex chosen as the origin. The circular profile exhibits the expected constant curvature, while the elliptical profiles become progressively more non-uniform as the axis ratio increases. In particular, the maximum curvature at the apex increases with ellipticity, whereas lower curvature values are obtained when

moving towards the lateral region of the tube. This geometrical analysis highlights that ellipticity does not simply modify the overall dimensions of the cladding tube, but also redistributes the curvature along the inner boundary.

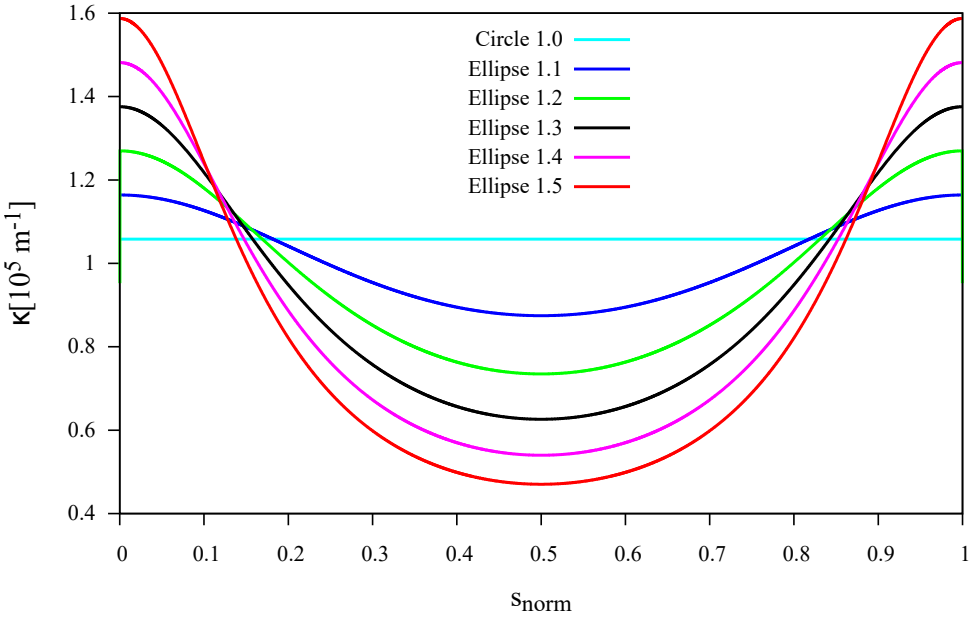


Figure 3.4: Inner-boundary curvature κ of the circular and elliptical tube profiles as a function of the normalized curvilinear coordinate s_{norm}.

3.4 Mode-Coupling-Loss Analysis

The effect of tube ellipticity on Mode-Coupling Loss is first examined by comparing the MCL spectra of the circular and elliptical configurations. Figure 3.5 reports a clear modification of the low-frequency falling edge when the tube shape is changed.

A first result emerging from the comparison is the shift of the decreasing MCL front towards lower normalized frequencies for all the investigated elliptical geometries with respect to the circular reference. Within the set of elliptical geometries, however, the displacement of the MCL falling edge is not monotonic with the axis ratio. As b/a increases from 1.1 to 1.3, the falling edge shifts progressively towards lower normalized frequencies. For larger axis ratios, the trend reverses: the falling edge moves again towards higher F, first slightly for $b/a = 1.4$ and more clearly for $b/a = 1.5$.

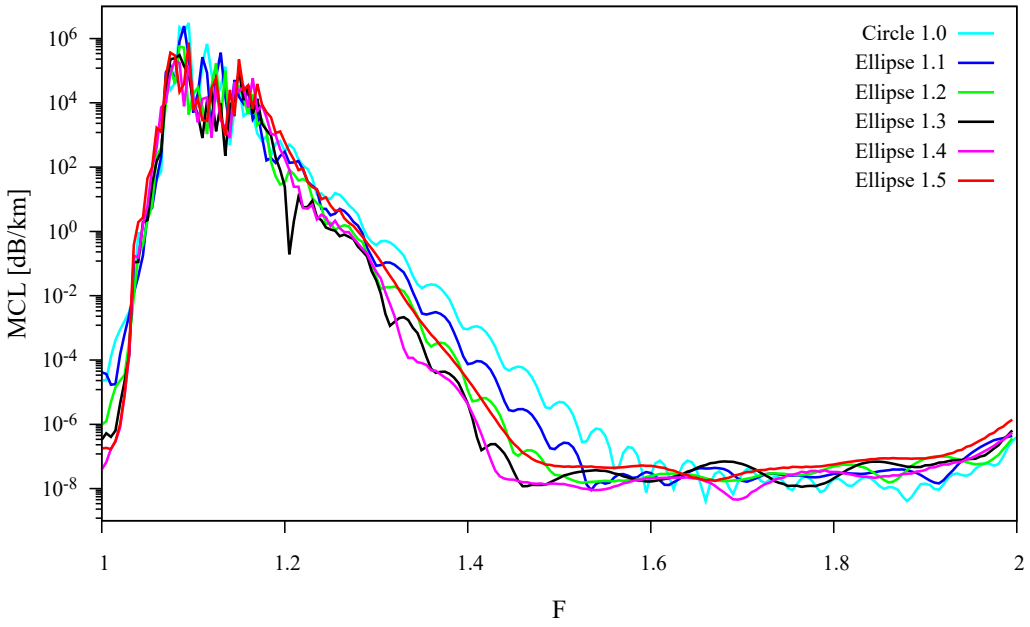


Figure 3.5: Mode-Coupling Loss spectra of the circular and elliptical tube geometries as a function of the normalized frequency F.

To provide a quantitative measure of the displacement of the MCL falling edge, a reference loss level of

$$\mathrm{MCL} = 10^{-2}\,\mathrm{dB/km} \tag{3.18}$$

is introduced as a common comparison criterion. For each geometry, F_{th} is defined as the normalized frequency at which the decreasing MCL front crosses this reference level. The resulting values are reported in Table 3.1.

To highlight the displacement of the MCL falling edge with respect to the circular reference, the relative threshold shift is defined as $\Delta F_{\mathrm{th}} = F_{\mathrm{th}}^{\mathrm{circ}} - F_{\mathrm{th}}$. The corresponding values are shown in Fig. 3.6.

The maximum enlargement is obtained for $b/a = 1.3$, after which the trend reverses for larger axis ratios.

Table 3.1: Normalized frequency F_{th} at which the decreasing MCL front crosses the reference level of 10^{-2} dB/km for the circular and elliptical tube geometries.

b/a	F_{th}
1.0	1.377
1.1	1.3418
1.2	1.3334
1.3	1.3055
1.4	1.3114
1.5	1.3289

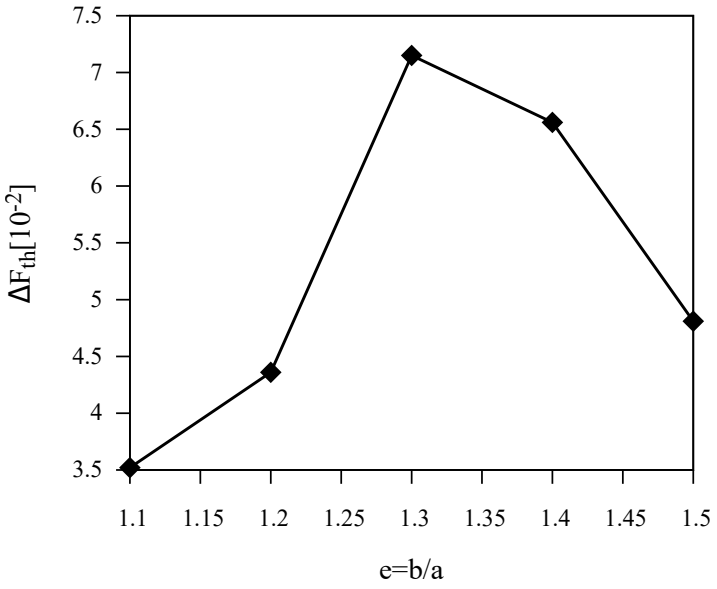


Figure 3.6: Normalized-frequency bandwidth enlargement ΔF_{th} at the MCL level of 10^{-2} dB/km with respect to the circular reference, as a function of the tube axis ratio b/a.

This comparison, however, refers to a specific MCL level and should not be interpreted as an absolute ordering of the different tube shapes, since the MCL curves are not related by a rigid spectral shift and may cross at lower loss levels. The non-monotonic evolution of the MCL falling edge cannot therefore be inferred from the axis ratio alone. Its interpretation requires examining how the tube shape modifies the modal properties involved in the FM–DM coupling mechanism.

3.5 Azimuthal Spectrum of the Fundamental Mode

The effect of tube geometry on the spatial distribution of the FM along the cladding boundary is investigated through the Azimuthal Fourier Decomposition introduced in Section 2.6. The analysis is performed for the y-polarized LP_{01}-like mode at the normalized frequency $F = 1.6$. To allow a direct comparison among the different geometries, the AFD coefficients are normalized with respect to their maximum amplitude,

$$\widetilde{R}_m = \frac{|R_m|}{\max_m |R_m|}, \tag{3.19}$$

and the quantity $|\widetilde{R}_m|^2$ is considered in the following analysis.

Figure 3.7 shows the normalized azimuthal spectra for the circular reference tube and for the elliptical geometries. The circular configuration exhibits the characteristic low-pass behavior of the FM spectrum, with most of the spectral content concentrated at low Fourier orders and a rapid decrease of the coefficients as m increases. For low Fourier orders, the spectral distributions remain relatively close, indicating that the dominant low-order components are only weakly affected by the elliptical deformation. Differences become progressively more evident at intermediate and high Fourier orders.

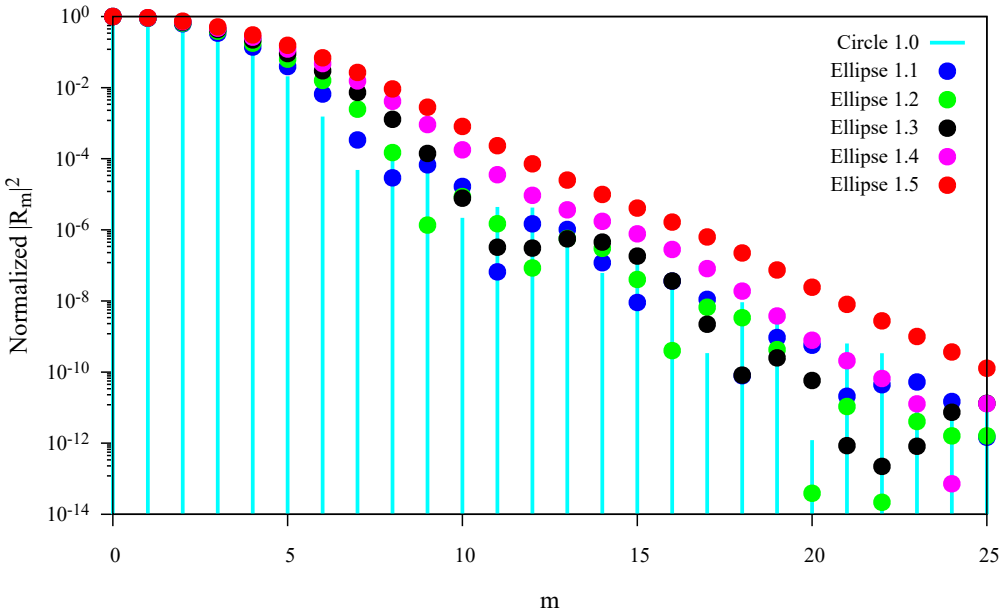


Figure 3.7: Squared normalized AFD coefficients $|\widetilde{R}_m|^2$ of the Fundamental Mode for the circular and elliptical tube geometries at $F = 1.6$.

The comparison of the different geometries shows that ellipticity redistributes the FM spectral content towards higher Fourier orders. This evolution, however, is neither uniform nor monotonic for the individual coefficients: the spectra exhibit local

minima and crossings whose positions depend on the tube geometry. In particular, the $b/a = 1.4$ and $b/a = 1.5$ geometries retain larger spectral amplitudes over a broader range of high-m components, with the $b/a = 1.5$ profile showing the broadest distribution. The effect of ellipticity is therefore better described as a redistribution and overall broadening of the azimuthal spectrum rather than as a uniform increase of its Fourier components.

To provide a compact measure of this spectral broadening, the RMS Fourier order m_{rms} is introduced as

$$m_{\mathrm{rms}} = \left[\frac{\sum_{m\geq 0} m^2 |\widetilde{R}_m|^2}{\sum_{m\geq 0} |\widetilde{R}_m|^2} \right]^{1/2} . \tag{3.20}$$

As shown in Figure 3.8, m_{rms} increases monotonically from 1.6756 for the circular tube to 2.4290 for $b/a = 1.5$. This trend indicates a progressive redistribution of the FM spectral weight towards higher Fourier orders as the tube axis ratio increases, although the individual Fourier coefficients do not evolve monotonically with the tube geometry. The FM azimuthal spectrum alone is therefore not sufficient to explain the evolution of the MCL spectrum. Since the coupling also depends on the spectral position of the Dielectric Modes, the effect of tube ellipticity on their cut-off frequencies is investigated in the following section.

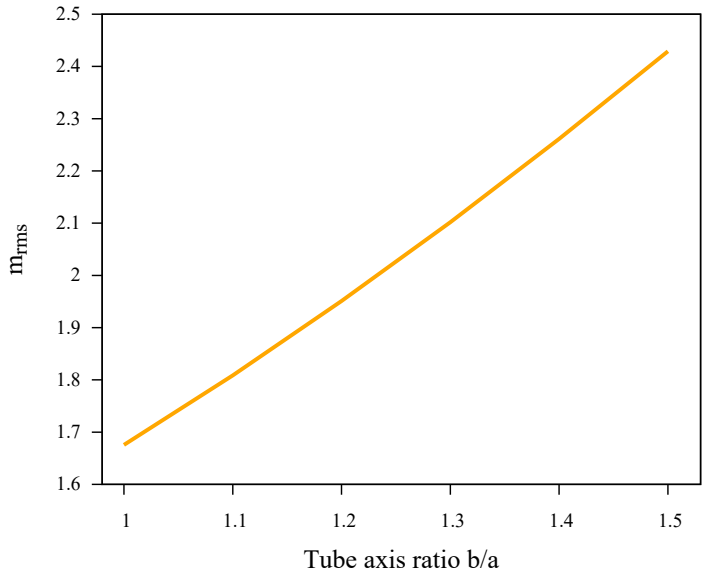


Figure 3.8: RMS Fourier order m_{rms} of the Fundamental-Mode azimuthal spectrum as a function of the tube axis ratio b/a.

3.6 Dielectric-Mode Cut-Off Frequencies

The second modal quantity considered in the analysis of Mode-Coupling Loss is the spectral distribution of the Dielectric-Mode cut-off frequencies.

Figure 3.9 shows the relation between the azimuthal order m and the normalized cut-off frequency F_c for the EH-polarized Dielectric Modes belonging to the $\nu = 2$ radial family. Only EH-polarized Dielectric Modes are reported in the following comparison, according to the analysis introduced in Section 3.2. The numerical analysis is performed over the complete transmission band $1 < F < 2$. In Fig. 3.9, the cut-off distribution is shown in the interval $1 < F < 1.6$, which contains the low-frequency side of the transmission band and the spectral region corresponding to the MCL falling edge.

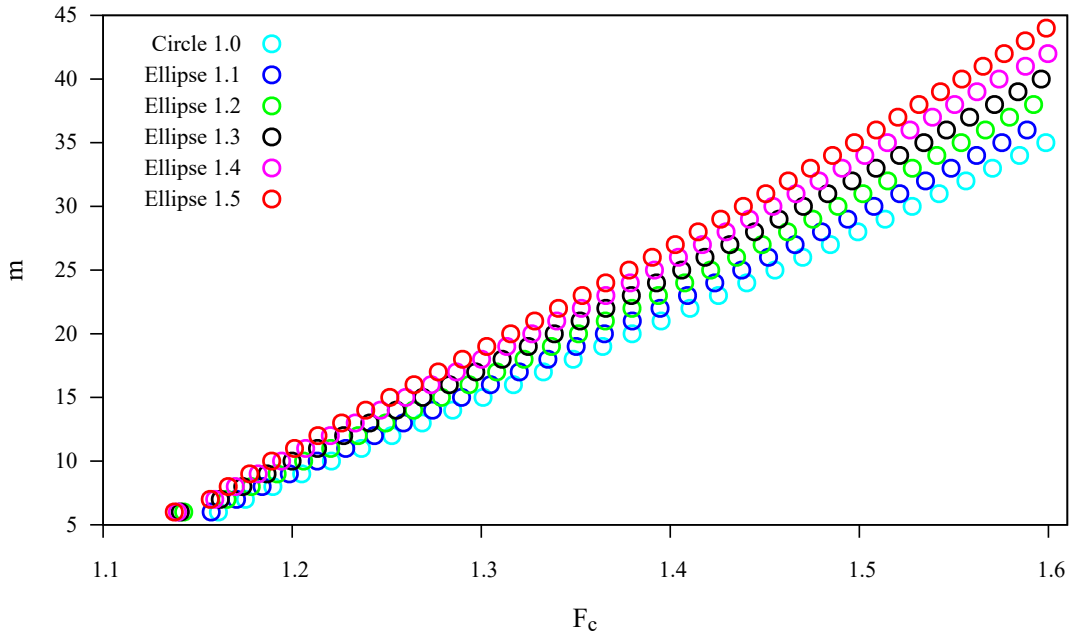


Figure 3.9: Azimuthal order m and corresponding normalized cut-off frequency F_c of the EH-polarized Dielectric Modes belonging to the $\nu = 2$ radial family, for the circular reference tube and the investigated elliptical profiles.

Two main effects can be observed. For a fixed azimuthal order, the cut-off frequency decreases as the tube axis ratio increases. At $m = 8$, for example, F_c decreases from 1.1898 for the circular tube to 1.1662 for $b/a = 1.5$, while at $m = 25$ it decreases from 1.4553 to 1.3782. The cut-off shift is not uniform with m. The difference between the circular tube and the $b/a = 1.5$ ellipse is about 0.0236 at $m = 8$ and increases to about 0.0771 at $m = 25$. The elliptical deformation thus produces both a shift of the considered cut-off sequence towards lower values of F and a compression of their spectral distribution. The same behavior can be observed

from the slope of the m–F_c branches.

As the axis ratio increases, the branches become steeper in the representation of Fig. 3.9; equivalently, a given increase in m corresponds to a progressively smaller increase in F_c.

To quantify this compression over the common modal sequence $8 \leq m \leq 25$, the spacing between consecutive cut-off frequencies is defined as

$$S(m, e) = F_c(m + 1, e) - F_c(m, e), \qquad m = 8, \ldots, 24, \tag{3.21}$$

where $e = b/a$. Figure 3.10 shows the evolution of $S(m, e)$ along the considered modal sequence. Although the spacing is not uniform with m, it decreases systematically as the tube axis ratio increases. The observed compression is therefore not limited to a different displacement of the two endpoints of the modal sequence, but results from a progressive reduction of the separation between consecutive cut-off frequencies throughout the considered range.

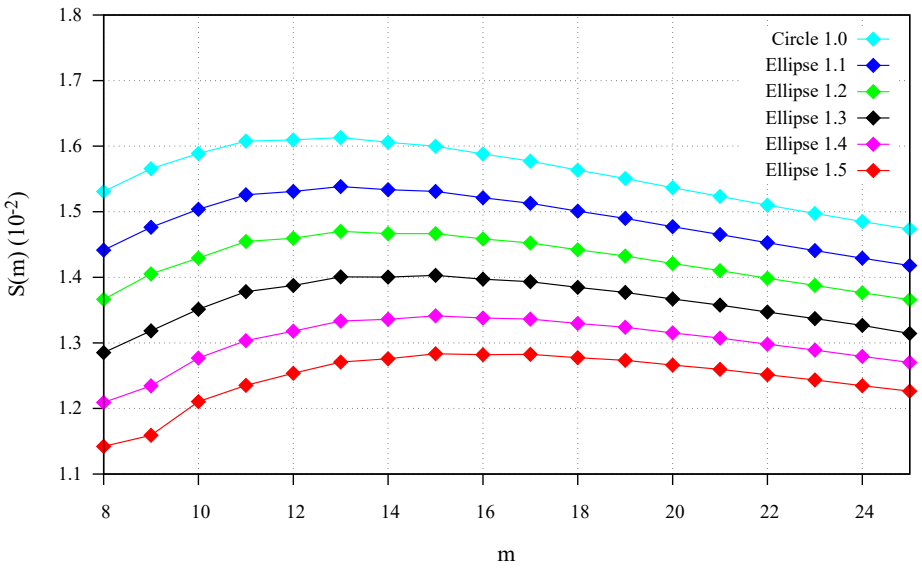


Figure 3.10: Local cut-off-frequency spacing $S(m, e)$ between consecutive EH-polarized Dielectric Modes of the $\nu = 2$ radial family, for the circular reference tube and the investigated elliptical profiles.

The overall compression of the same modal sequence can then be quantified through its total spectral width,

$$W(e) = \sum_{m=8}^{24} S(m, e) = F_c(25, e) - F_c(8, e). \tag{3.22}$$

The corresponding values are reported in Table 3.2.

The spectral width decreases monotonically from $W = 0.2655$ for the circular tube to $W = 0.2120$ for $b/a = 1.5$, corresponding to a reduction of about 20.2%.

The same sequence of azimuthal orders therefore occupies a progressively narrower frequency interval as the tube ellipticity increases.

Table 3.2: Cut-off frequencies at $m = 8$ and $m = 25$ and spectral width W for the circular reference tube and the investigated elliptical profiles.

b/a	$F_c(8)$	$F_c(25)$	W
1.0	1.189777	1.455311	0.265534
1.1	1.184065	1.437780	0.253715
1.2	1.178374	1.421352	0.242978
1.3	1.173875	1.405990	0.232115
1.4	1.169927	1.391618	0.221691
1.5	1.166152	1.378166	0.212014

3.7 Combined Interpretation of the FM Azimuthal Spectrum and DM Cut-Offs

The analyses presented in the previous sections show that tube ellipticity modifies both modal quantities involved in Mode-Coupling Loss. The Dielectric-Mode cut-off sequence shifts towards lower normalized frequencies and becomes progressively compressed as the axis ratio increases, whereas the Fundamental-Mode azimuthal spectrum undergoes a non-uniform redistribution of its Fourier components. Neither quantity considered separately is sufficient to describe the spectral evolution of the MCL falling edge. As discussed in Section 2.6, within a given radial family the MCL can be interpreted as the superposition of contributions associated with the Dielectric Modes. Their spectral positions are well approximated by the corresponding cut-off frequencies, whereas the squared Fundamental-Mode AFD coefficients provide information on the relative harmonic content available for coupling [4], [7].

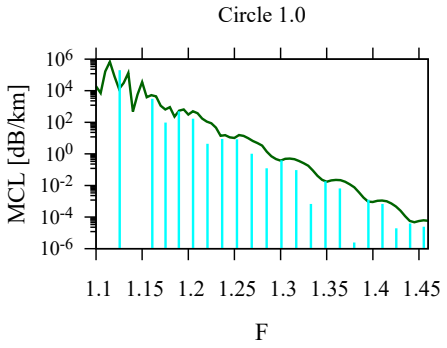
For the elliptical profiles considered here, the correspondence between the DM azimuthal order and its dominant Fourier harmonic was also verified numerically on representative EH-polarized modes. For all the examined geometries, the DM spectra remain strongly dominated by the components at orders $\pm m$, while the neighboring Fourier components have substantially smaller amplitudes. Therefore, the azimuthal order m assigned to each DM also identifies its dominant Fourier harmonic for the elliptical profiles considered here. The two modal quantities can thus be combined by associating each FM Fourier coefficient of order m with the cut-off frequency of the Dielectric Mode having the same azimuthal order,

$$\left(m, |\widetilde{R}_m(F=1.6)|^2\right) \longrightarrow \left(F_c(m), |\widetilde{R}_m(F=1.6)|^2\right). \tag{3.23}$$

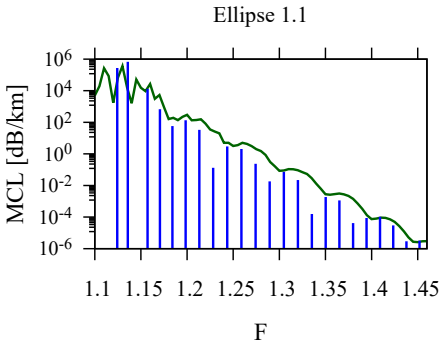
The AFD coefficients are those reported in Section 3.5, evaluated at $F = 1.6$. Equation (3.23) preserves their amplitudes and assigns each FM harmonic to the spectral position of the corresponding DM. In this representation, $F_c(m)$ provides an estimate of the spectral position of the FM–DM interaction, whereas $|\widetilde{R}_m|^2$ represents the relative FM harmonic content associated with the corresponding azimuthal order.

The comparison is restricted to the common sequence $8 \leq m \leq 25$ of EH-polarized Dielectric Modes belonging to the $\nu = 2$ radial family. Figure 3.11 shows that the same spectral region is associated with different azimuthal orders as the tube axis ratio is varied. The vertical bars should therefore not be interpreted as point values of MCL. Their vertical scale is arbitrary and independently chosen for each geometry; they provide a representation of the relative harmonic contributions involved in the spectral evolution of MCL.

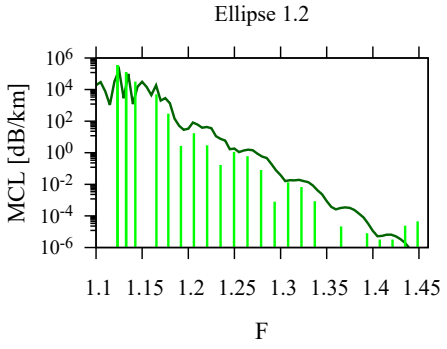
This follows from the displacement and compression of the DM cut-off sequence



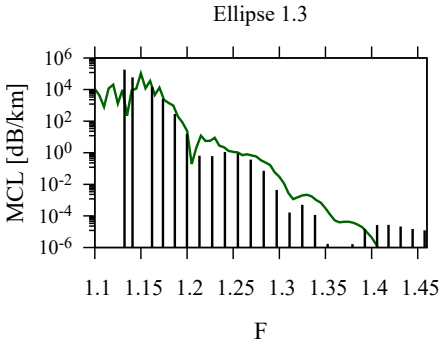
(a) $b/a = 1.0$.



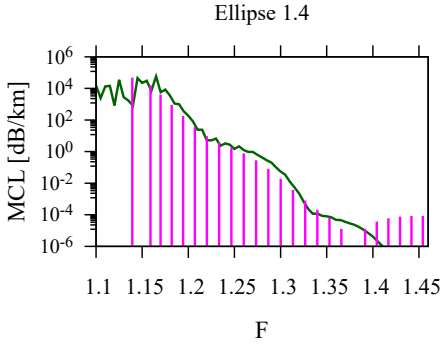
(b) $b/a = 1.1$.



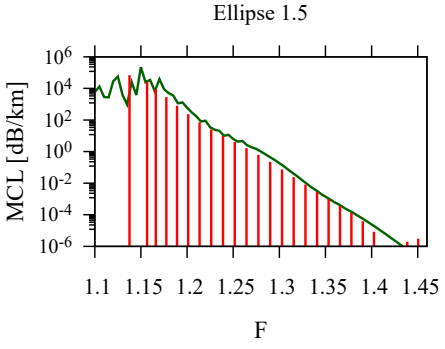
(c) $b/a = 1.2$.



(d) $b/a = 1.3$.



(e) $b/a = 1.4$.



(f) $b/a = 1.5$.

Figure 3.11: Mode-Coupling Loss spectra and squared normalized AFD coefficients $|\widetilde{R}_m|^2$ mapped onto the cut-off frequencies of the corresponding EH-polarized Dielectric Modes. The AFD coefficients, evaluated at $F = 1.6$, are independently rescaled in each panel for visual comparison. The comparison focuses on the MCL falling-edge region.

described in Section 3.6. Consequently, a comparison of the AFD coefficients at fixed m does not necessarily compare FM components associated with the same portion of the MCL spectrum. The combined quantity $\left(F_c(m), |\widetilde{R}_m|^2\right)$ therefore provides a more direct representation of the simultaneous changes in DM spectral position and FM harmonic content.

A representative example is provided by the $b/a = 1.3$ and $b/a = 1.4$ geometries, which cross the reference MCL level of 10^{-2} dB/km at $F \simeq 1.3055$ and $F \simeq 1.3114$, respectively. In the same spectral region, the closest mapped contributions correspond to the $m = 18$ mode of the $b/a = 1.3$ geometry,

$$F_c \simeq 1.3110, \qquad |\widetilde{R}_{18}|^2 \simeq 9.1 \times 10^{-6}, \tag{3.24}$$

and to the $m = 19$ mode of the $b/a = 1.4$ geometry,

$$F_c \simeq 1.3135, \qquad |\widetilde{R}_{19}|^2 \simeq 6.1 \times 10^{-5}. \tag{3.25}$$

Thus, in this spectral region, the two geometries are characterized not only by different DM cut-off positions but also by different normalized FM harmonic contents. In particular, the contribution mapped for $b/a = 1.3$ occurs at a slightly lower frequency and is associated with a smaller normalized FM AFD coefficient than the neighboring contribution of the $b/a = 1.4$ geometry.

The present mapping is used to compare the spectral positions and relative harmonic weights of the coupling contributions; a quantitative reconstruction of their absolute resonance profiles would instead require the complete Coupled-Mode-Theory description, including the propagation-constant mismatch $\Delta\beta$, the differential attenuation $\Delta\alpha$, and the coupling coefficient κ [3].

3.8 Geometrical Interpretation in Terms of Boundary Spatial Wavenumber

The analyses presented above have been expressed in terms of the integer azimuthal order m. As described in Section 3.2, for the non-circular profiles the field variation along the tube boundary is evaluated using the curvilinear coordinate s. Since the investigated geometries have different boundary lengths, the same azimuthal order does not correspond to the same spatial oscillation scale along the tube contour.

Let P denote the total inner-boundary perimeter. The normalized curvilinear coordinate can be written as

$$\phi = \frac{2\pi s}{P}. \tag{3.26}$$

A Fourier harmonic of order m therefore takes the form

$$\exp(im\phi) = \exp\left(i\frac{2\pi m}{P}s\right), \tag{3.27}$$

which defines the boundary spatial wavenumber

$$k_s = \frac{2\pi m}{P}. \tag{3.28}$$

For a given geometry, consecutive azimuthal orders are consequently separated by

$$\Delta k_s = \frac{2\pi}{P}. \tag{3.29}$$

Since the tube perimeter increases with the axis ratio, the same integer order m is associated with a smaller k_s as the ellipticity increases, while the spacing between consecutive spatial harmonics becomes progressively smaller. For the FM, m identifies the Fourier harmonic order. For the Dielectric Modes, it identifies the azimuthal order of the mode and, as verified in Section 3.7, the corresponding Fourier spectrum remains strongly dominated by the components at $q = \pm m$. The boundary spatial wavenumber can therefore be used to compare the two modal quantities on the same physical spatial scale.

The effect of this spatial rescaling is first examined for the Dielectric-Mode cut-off frequencies. Figure 3.12 reports the EH-polarized DM cut-offs in the (F_c, k_s) plane.

In the m–F_c representation of Section 3.6, the different geometries show a clear separation: at fixed m, the cut-off frequencies shift towards lower values and the modal sequence becomes progressively compressed as b/a increases. When the same modes are represented in terms of k_s, the different sequences become distributed along nearly the same $F_c(k_s)$ trend. The points do not coincide mode by mode,

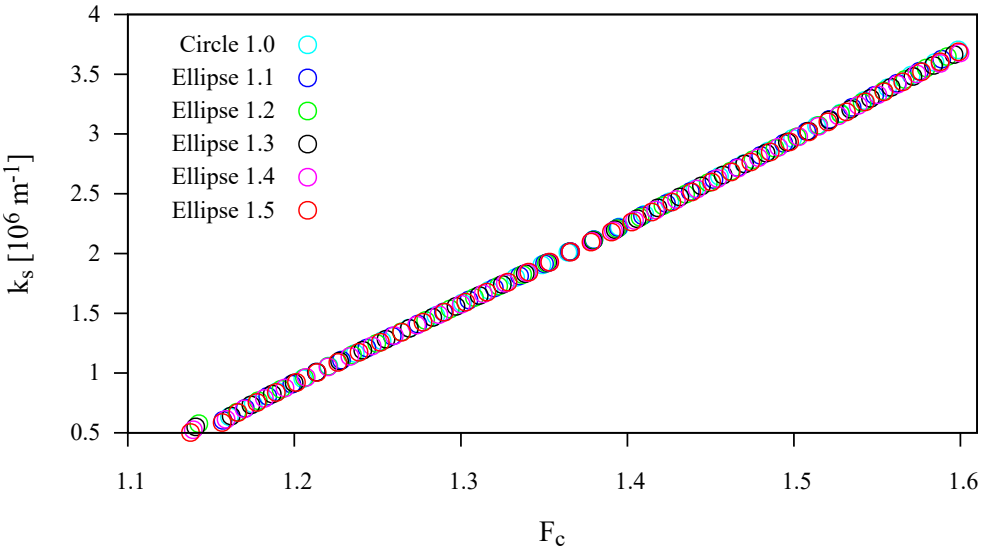


Figure 3.12: Boundary spatial wavenumber $k_s = 2\pi m/P$ associated with the azimuthal order of the EH-polarized Dielectric Modes as a function of the normalized cut-off frequency F_c for the circular and elliptical tube geometries.

since each geometry has a different perimeter and therefore a different discrete set of spatial wavenumbers. Nevertheless, modes associated with similar values of k_s exhibit similar cut-off frequencies even when they correspond to different azimuthal orders. To quantify this alignment, the RMS dispersion among the six cut-off sequences was evaluated with respect to their mean distribution, comparing the curves at equal m and, after interpolation, at equal k_s. The dispersion decreases from 1.88×10^{-2} to 3.67×10^{-4}, corresponding to a reduction of about 98.1%.

The separation observed between the cut-off sequences in the m–F_c representation is therefore almost completely removed when the modal order is expressed in terms of its physical spatial scale along the boundary. This also explains the compression observed in Section 3.6: as the tube perimeter increases, consecutive azimuthal orders correspond to more closely spaced spatial wavenumbers and, consequently, to more closely spaced cut-off frequencies. A small residual spread remains after the transformation, showing that the perimeter does not completely determine the cut-off frequencies and that a dependence on the detailed tube profile is still present.

The same change of variable can be applied to the Fundamental-Mode azimuthal spectrum introduced in Section 3.5. The transformation does not modify the AFD coefficients, but only their position on the horizontal axis. Harmonics having the same integer order m in different geometries therefore occur at different values of k_s, whereas harmonics with different integer orders can correspond to similar spatial wavenumbers.

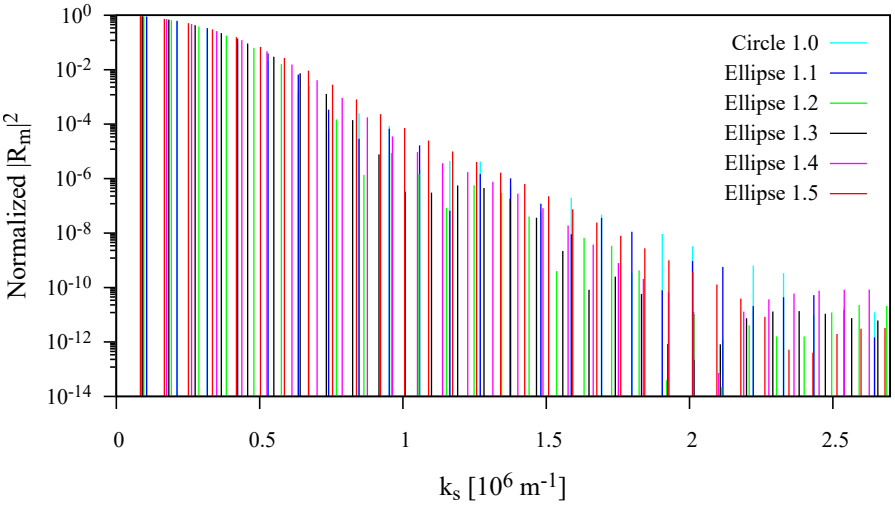


Figure 3.13: Squared normalized Fundamental-Mode AFD coefficients $|\widetilde{R}_m|^2$ as a function of the boundary spatial wavenumber $k_s = 2\pi m/P$ for the circular and elliptical tube geometries. Each impulse retains the amplitude of the corresponding Fourier coefficient, while its horizontal position is determined by the spatial wavenumber associated with that harmonic.

Figure 3.13 therefore provides the same normalized FM Fourier coefficients as the m-domain representation, but expressed in terms of their physical oscillation scale along the tube boundary. Unlike the DM cut-off sequences, the FM spectra do not show a comparable alignment after the transformation. The same comparison was performed for the FM spectra using $\log_{10}|\widetilde{R}_m|^2$, after interpolation on a common k_s grid. The RMS dispersion decreases from approximately 0.953 to 0.685 decades, corresponding to a reduction of about 28.1%. The spatial rescaling therefore reduces the differences only partially, while a significant geometry-dependent redistribution of the FM azimuthal spectrum remains.

The comparison between Figures 3.12 and 3.13 therefore highlights a different response of the two modal quantities to the same spatial rescaling. The variation of the DM cut-off distribution is largely accounted for by the change in the spatial scale associated with the different tube perimeters, whereas the FM azimuthal spectrum retains a marked dependence on the tube geometry after this effect has been taken into account.

3.9 Conclusions

The effect of a global elliptical deformation of the cladding tubes has been investigated by varying the axis ratio from $b/a = 1$ to $b/a = 1.5$ while keeping the remaining fiber parameters unchanged. The results show that the tube shape produces a marked modification of Mode-Coupling Loss and, in particular, of the low-frequency falling edge of the considered Transmission Band. The displacement is not monotonic with ellipticity, with the lowest crossing at the reference level of 10^{-2} dB/km obtained for $b/a = 1.3$.

The modal analysis shows that this behavior cannot be attributed to a single geometrical or modal quantity. The Fundamental-Mode azimuthal spectrum undergoes a non-uniform redistribution with the tube shape, whereas the EH Dielectric-Mode cut-off sequence shifts monotonically towards lower normalized frequencies and becomes progressively compressed. Mapping the FM AFD coefficients onto the corresponding DM cut-off frequencies provides the combined spectral information required to interpret the evolution of the MCL falling edge.

The spatial-wavenumber representation further clarifies the geometrical origin of these changes. When the azimuthal order is rescaled according to $k_s = 2\pi m/P$, the DM cut-off sequences of the different elliptical geometries become strongly aligned in the (F_c, k_s) plane, showing that the change of the global boundary length accounts for a substantial part of their separation in the m representation. The FM azimuthal spectra, on the other hand, retain significant geometry-dependent differences after the same rescaling.

These results suggest a different sensitivity of the two modal quantities to global and local features of the tube profile. To investigate this aspect more directly, the following chapter considers tube geometries in which only the core-facing portion of the boundary is locally modified, while the global dimensions of the corresponding starting ellipse are preserved.

Chapter 4

Local Modification of the Core-Facing Tube Apex

Elliptical deformation modifies the entire inner-boundary profile of the cladding tubes and, consequently, the curvature distribution along the dielectric boundary. Since these geometrical variations occur simultaneously when the tube axis ratio is changed, the analysis of elliptical geometries alone does not allow the influence of the local core-facing geometry to be separated from that of the overall tube shape. Particular attention is therefore devoted to the tube region directly facing the hollow core, where the interaction between the Fundamental Mode and the Dielectric Modes takes place. The $b/a = 1.3$ ellipse, which exhibits the lowest-frequency crossing of the reference MCL level considered in Chapter 3, is selected as the reference configuration. The core-facing regions of ellipses with different axis ratios are then locally reshaped towards the curvature distribution of this reference profile while preserving their original overall dimensions. The modified profiles are first characterized through their boundary-curvature distributions. Their Mode-Coupling Loss, Fundamental-Mode azimuthal spectra, and Dielectric-Mode cut-off frequencies are then compared to determine how the local profile modification affects the modal quantities governing MCL.

4.1 Reference Geometry and Local Modification

The $b/a = 1.3$ ellipse is used as the reference profile for the construction of the locally modified geometries. Starting from the $b/a = 1.1$, 1.2, 1.4, and 1.5 ellipses, the inner boundary is reshaped within a localized region surrounding the core-facing apex. The modification is designed to make the curvature distribution in this region approach that of the reference profile, while preserving the overall dimensions of each starting ellipse. Accordingly, the $b/a = 1.1$ and 1.2 geometries are locally sharpened, whereas the $b/a = 1.4$ and 1.5 geometries are locally flattened.

The local modification is introduced through a Gaussian deformation centred at the core-facing apex. The angular coordinate θ is defined such that $\theta = 0$ corresponds to the apex, and the normalized Gaussian profile is written as

$$g(\theta) = \exp\left(-\frac{\theta^2}{2\sigma^2}\right), \tag{4.1}$$

where σ is the standard deviation of the Gaussian profile and determines the angular extension of the perturbed region. The displacement applied to the original elliptical boundary is

$$d(\theta) = \delta g(\theta), \tag{4.2}$$

where δ is the amplitude of the Gaussian perturbation, so that $d(0) = \delta$ before the subsequent recentering and rescaling of the profile. The Gaussian deformation is applied only to the y-coordinate of the parametric elliptical profile:

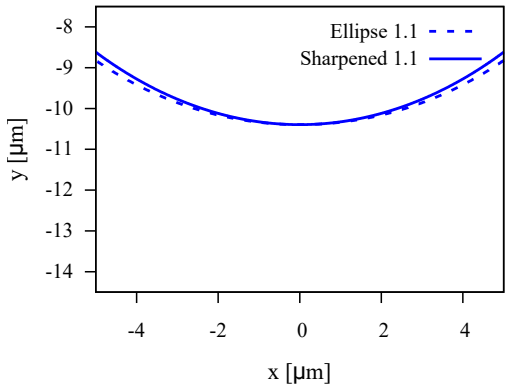
$$y_{\mathrm{mod}}(\theta) = y_{\mathrm{ell}}(\theta) \pm d(\theta), \tag{4.3}$$

where the positive sign generates a flattened profile, whereas the negative sign generates a sharpened profile.

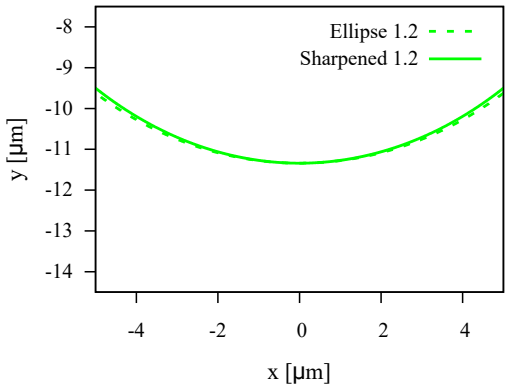
For each initial ellipticity, δ and σ are independently adjusted so that the resulting curvature profile follows that of the $b/a = 1.3$ reference ellipse over the core-facing region. The Gaussian deformation modifies the extrema of the original contour; the resulting profile is therefore recentered and rescaled along the two transverse directions to restore the original dimensions $2a$ and $2b$ of the corresponding starting ellipse. In this way, the global dimensions associated with each axis ratio are preserved while the geometrical modification remains concentrated in the core-facing region. The parameters adopted for the different geometries are reported in Table 4.1. The resulting tube profiles are shown in Figure 4.1, where each locally modified geometry is compared with the corresponding original ellipse.

Table 4.1: Parameters of the Gaussian deformation applied to the elliptical tube profiles.

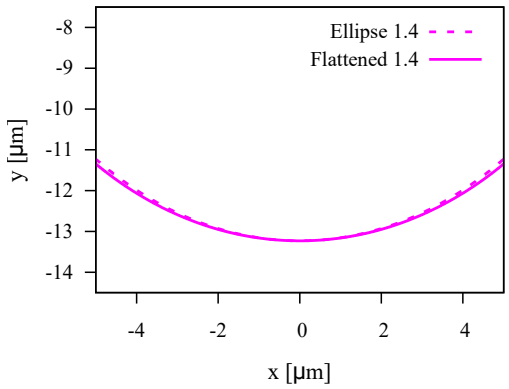
Initial axis ratio b/a	Profile	δ [μm]	σ [rad]
1.1	Sharpened	0.52	0.490
1.2	Sharpened	0.56	0.660
1.4	Flattened	1.00	0.860
1.5	Flattened	1.80	0.825



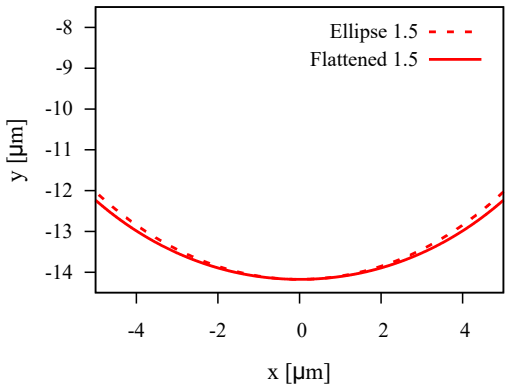
(a) $b/a = 1.1$: sharpened profile.



(b) $b/a = 1.2$: sharpened profile.



(c) $b/a = 1.4$: flattened profile.



(d) $b/a = 1.5$: flattened profile.

Figure 4.1: Comparison between the original elliptical inner-boundary profiles and the corresponding locally modified geometries in the core-facing region.

4.2 Boundary Curvature Analysis

The curvature at the core-facing apex is first considered as a scalar measure of the initial geometrical difference between each elliptical profile and the $b/a = 1.3$ reference configuration. For an elliptical inner boundary, the apex curvature is

$$\kappa_{\text{apex}} = \frac{b}{a^2} = \frac{e}{a}, \tag{4.4}$$

where $e = b/a$. Since the semi-minor axis is fixed at $a = 9.45$ μm, the apex curvature increases with the tube axis ratio. The $b/a = 1.3$ reference ellipse is characterized by

$$\kappa_{\text{ref}} = 1.376 \times 10^5 \text{ m}^{-1}. \tag{4.5}$$

The relative change in apex curvature required for each original ellipse to reach the reference value is defined as

$$\frac{\Delta\kappa_{\text{req}}}{\kappa_{\text{apex}}} = \frac{\kappa_{\text{ref}} - \kappa_{\text{apex}}}{\kappa_{\text{apex}}} \times 100. \tag{4.6}$$

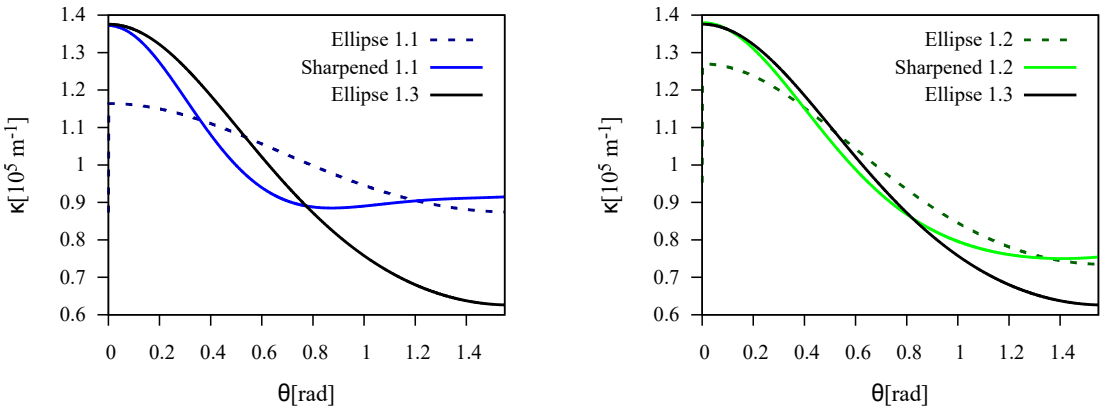
This quantity provides a direct indication of how far the curvature of each initial ellipse is from that of the reference geometry at the centre of the region subsequently modified. A positive value indicates that the curvature must be increased to reach the reference value, whereas a negative value indicates that it must be reduced.

Table 4.2: Apex curvature of the original elliptical profiles and relative change required to reach the $b/a = 1.3$ reference value.

Initial axis ratio b/a	κ_{apex} [m^{-1}]	Required relative apex-curvature change
1.1	1.164×10^5	+18.18%
1.2	1.270×10^5	+8.33%
1.3	1.376×10^5	Reference
1.4	1.481×10^5	−7.14%
1.5	1.587×10^5	−13.33%

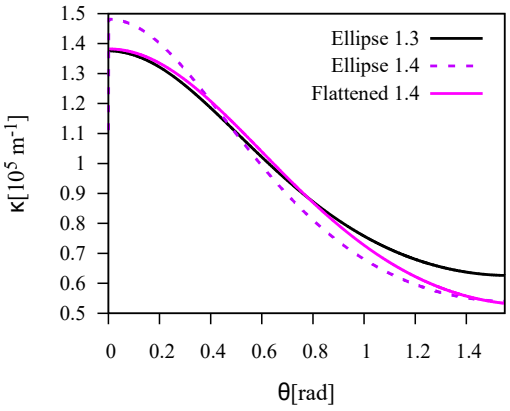
The $b/a = 1.1$ and 1.2 ellipses therefore require an increase of the curvature in the core-facing region and are locally sharpened, whereas the $b/a = 1.4$ and 1.5 ellipses require a reduction and are locally flattened. The apex values reported in Table 4.2 are used only to quantify the initial mismatch with respect to the reference geometry. The Gaussian deformation introduced in Section 4.1 is instead adjusted with the broader objective of reproducing the curvature distribution of the $b/a = 1.3$ ellipse in the region surrounding the core-facing apex.

Figure 4.2 compares each sharpened or flattened profile with the $b/a = 1.3$ reference ellipse. The parametric angular coordinate θ is defined consistently with Section 4.1, with $\theta = 0$ corresponding to the core-facing tube apex.

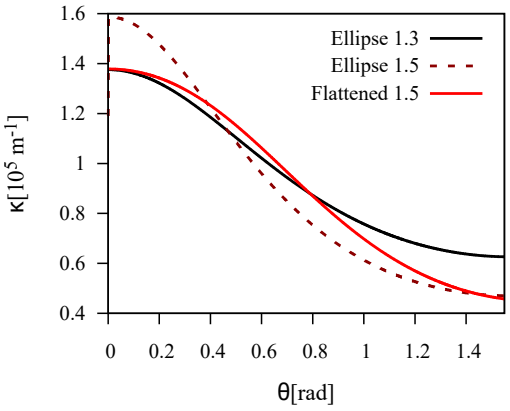


(a) Sharpened $b/a = 1.1$.

(b) Sharpened $b/a = 1.2$.



(c) Flattened $b/a = 1.4$.



(d) Flattened $b/a = 1.5$.

Figure 4.2: Comparison between the curvature distributions of the original elliptical profiles, the corresponding locally modified geometries, and the $b/a = 1.3$ reference ellipse in the core-facing region.

All the modified profiles exhibit a curvature close to that of the reference ellipse in the region surrounding the core-facing apex. For the profiles showing the closest agreement, the reference curvature trend is approximately reproduced up to $\theta \simeq 0.8$ rad ($\sim 46°$) from the apex. Beyond this region, differences progressively emerge as the local geometry recovers the characteristics associated with the corresponding starting ellipticity. In particular, the sharpened $b/a = 1.2$ and flattened $b/a = 1.4$ profiles remain comparatively closer to the reference curvature over a wider angular range, whereas larger deviations are observed for the $b/a = 1.1$ and $b/a = 1.5$ cases. This set of geometries can therefore be used to investigate how the modification of the local core-facing curvature affects the confinement properties while retaining different overall tube profiles.

4.3 Mode-Coupling-Loss Analysis

The effect of the local modification of the core-facing tube profile is investigated through the Mode-Coupling Loss spectra. Figure 4.3 compares the MCL spectra of all the modified profiles with that of the $b/a = 1.3$ reference geometry over the normalized frequency range $1 < F < 2$.

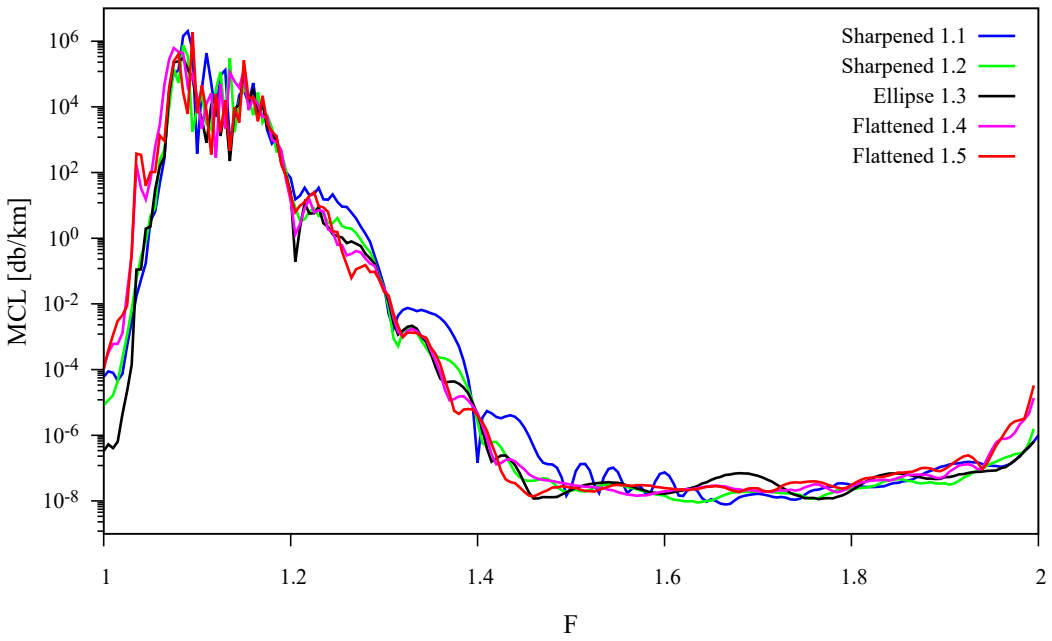


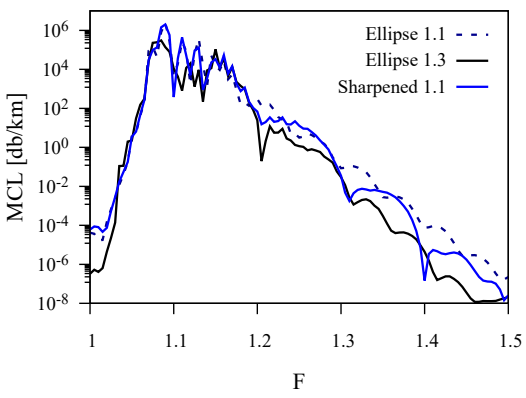
Figure 4.3: Mode-Coupling Loss spectra of the locally modified tube profiles and of the $b/a = 1.3$ reference ellipse.

The comparison reveals that, despite the different overall tube geometries, the local modification produces a strong similarity in the low-frequency falling edge of the MCL spectra. The sharpened $b/a = 1.2$ and the flattened $b/a = 1.4$ and 1.5 profiles follow the $b/a = 1.3$ reference closely over this spectral region. The sharpened $b/a = 1.1$ profile represents the main exception, showing a more structured response characterized by pronounced resonant peaks.

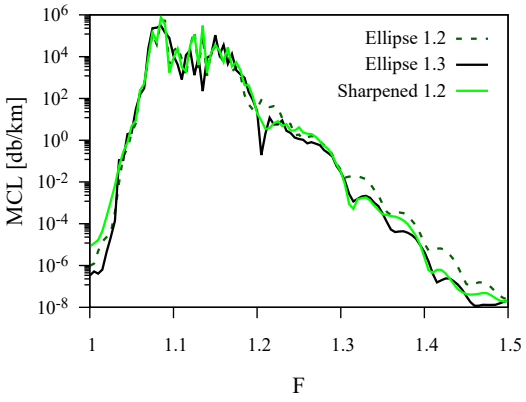
To isolate the effect of the local deformation from that of the original ellipticity, each modified profile is compared in Fig. 4.4 with both its corresponding ellipse and the $b/a = 1.3$ reference geometry. For $b/a = 1.1$, the local sharpening does not produce a pronounced displacement of the MCL falling edge with respect to the original ellipse but the modified profile is closer to the $b/a = 1.3$ reference. More importantly, the sharpening introduces a series of pronounced resonant peaks, which make the MCL spectrum considerably more structured than those of the other modified geometries. As shown in Section 4.2, the $b/a = 1.1$ ellipse exhibits the largest relative mismatch in apex curvature with respect to the reference geometry. The possible relation between

the larger curvature correction required for this profile and the additional resonant features cannot, however, be established from the loss spectrum alone. A different behavior is observed for $b/a = 1.2$. The MCL falling edge of the original ellipse is clearly displaced with respect to that of the reference geometry. After sharpening the core-facing region, the loss curve shifts toward the $b/a = 1.3$ configuration and follows it closely over most of the decreasing-loss region. For $b/a = 1.4$, the original elliptical geometry already exhibits a falling edge relatively close to that of the $b/a = 1.3$ reference. The local flattening further reduces the residual difference, leading to an almost coincident MCL evolution over the low-frequency falling edge. The effect becomes particularly evident again for $b/a = 1.5$. In this case, the original elliptical profile exhibits a MCL falling edge markedly displaced from the $b/a = 1.3$ curve. After the local flattening, the MCL response is strongly shifted toward the reference configuration, despite the modified profile retaining the overall dimensions of the $b/a = 1.5$ parent ellipse.

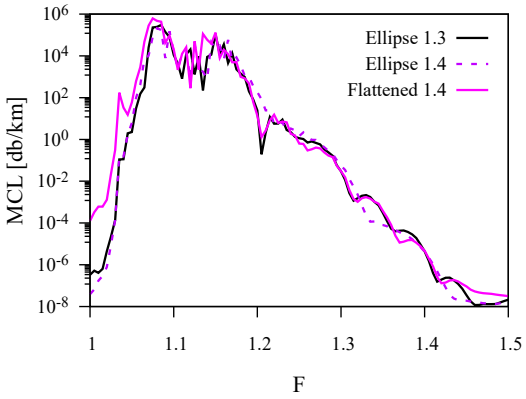
The physical origin of these results is investigated in the following sections by analyzing separately the two quantities governing the core–cladding modal interaction: the AFD coefficients of the Fundamental Mode and the cut-off frequencies of the Dielectric Modes.



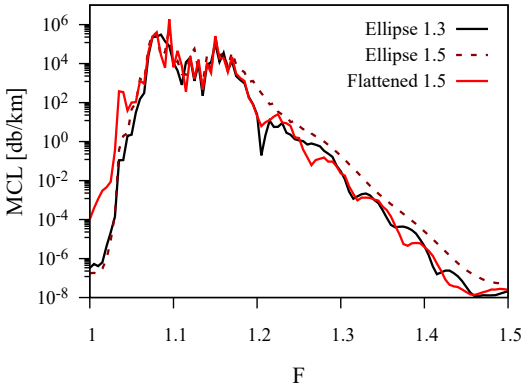
(a) $b/a = 1.1$ and sharpened $b/a = 1.1$.



(b) $b/a = 1.2$ and sharpened $b/a = 1.2$.



(c) $b/a = 1.4$ and flattened $b/a = 1.4$.



(d) $b/a = 1.5$ and flattened $b/a = 1.5$.

Figure 4.4: Mode-Coupling Loss spectra in the low-frequency falling-edge region for the original elliptical profiles, the corresponding locally modified geometries, and the $b/a = 1.3$ reference ellipse: (a) sharpened $b/a = 1.1$, (b) sharpened $b/a = 1.2$, (c) flattened $b/a = 1.4$, and (d) flattened $b/a = 1.5$. For each comparison, the parent ellipse is shown with a dashed line, whereas the corresponding locally modified profile is shown with a solid line.

4.4 Azimuthal Fourier Decomposition of the Fundamental Mode

The effect of the local profile modification on the azimuthal content of the Fundamental Mode is investigated through the AFD introduced in Section 2.6. The squared normalized coefficients $|\widetilde{R}_m|^2$ are evaluated at $F = 1.6$ using the same procedure and normalization adopted in Section 3.5.

Figure 4.5 compares the resulting spectra for the locally modified profiles with that of the $b/a = 1.3$ reference ellipse.

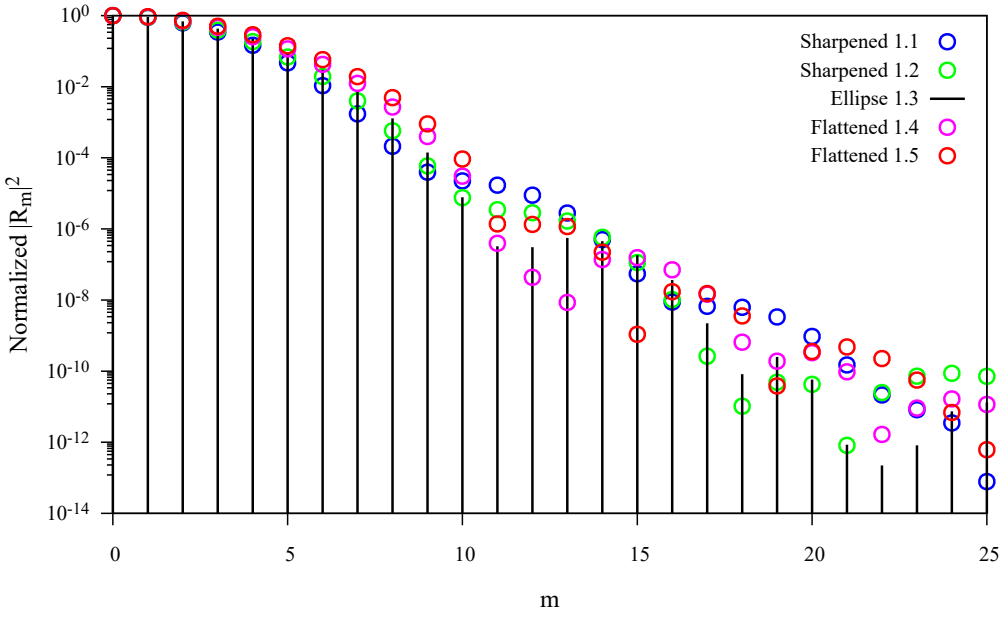


Figure 4.5: Squared normalized AFD coefficients of the Fundamental Mode for the locally modified tube profiles and the $b/a = 1.3$ reference ellipse, evaluated at $F = 1.6$.

To identify the effect of the local deformation more clearly, each modified profile is compared in Fig. 4.6 with both its original elliptical geometry and the $b/a = 1.3$ reference.

For $b/a = 1.1$, the sharpening produces a redistribution of the AFD coefficients, although no uniform convergence toward the $b/a = 1.3$ distribution is observed. Some harmonics approach the reference values, whereas others retain or develop larger differences. This less regular response is consistent with the particular behavior observed in the MCL spectrum of the sharpened $b/a = 1.1$ profile, which is characterized by pronounced resonant features.

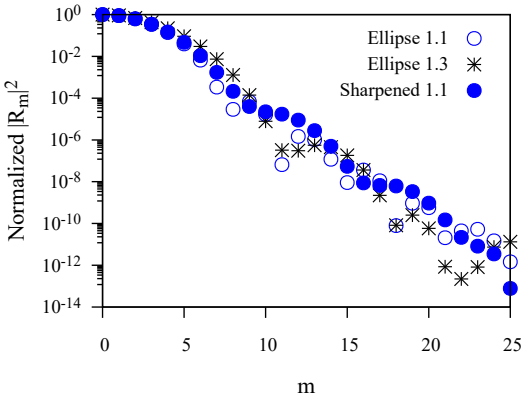
For $b/a = 1.2$, the effect of the local sharpening is considerably clearer. Several low- and intermediate-order coefficients of the original ellipse differ from those of the $b/a = 1.3$ geometry, whereas the corresponding coefficients of the sharpened

profile move toward the reference distribution. The modification of the FM azimuthal content therefore accompanies the displacement of the MCL falling edge observed in Section 4.3.

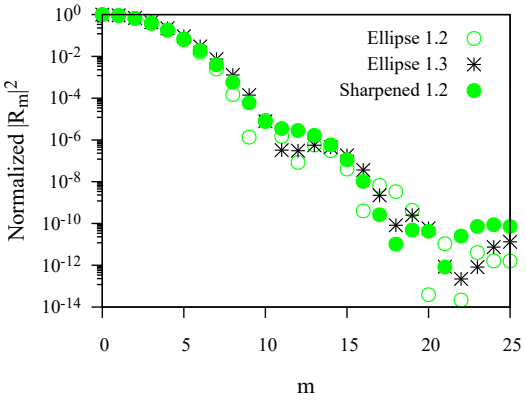
For $b/a = 1.4$, the original and reference distributions are already relatively close at low azimuthal orders. The local flattening mainly affects the intermediate-order harmonics and brings several of them into closer agreement with the $b/a = 1.3$ coefficients.

The most pronounced redistribution is observed for $b/a = 1.5$. Over a broad range of intermediate azimuthal orders, the original ellipse exhibits AFD coefficients substantially larger than those of the $b/a = 1.3$ reference. Flattening the core-facing region strongly suppresses these components, bringing the resulting distribution close to that of the reference geometry.

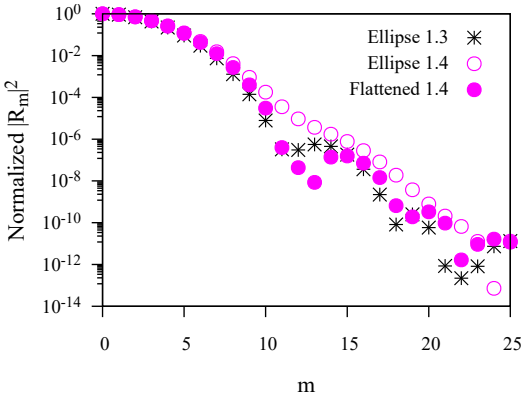
The pairwise comparisons therefore show that the local core-facing geometry has a strong influence on the azimuthal content of the Fundamental Mode. In particular, the 1.5 case shows that a local modification of the tube boundary can substantially redistribute the FM harmonic content and drive their distribution toward that of the $b/a = 1.3$ reference, while preserving the overall dimensions of the corresponding parent ellipse. The evolution of the AFD coefficients is consistent with the corresponding changes observed in the MCL spectra and demonstrates the strong sensitivity of the FM azimuthal content to the local core-facing tube profile. However, the AFD coefficients describe the relative FM harmonic content available for coupling and do not alone determine the spectral position of the corresponding core–cladding interactions. As discussed in Chapter 3, these positions can be approximated by the cut-off frequencies of the corresponding Dielectric Modes.



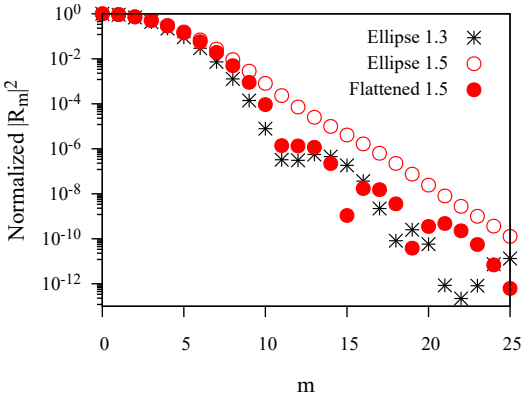
(a) $b/a = 1.1$ and sharpened $b/a = 1.1$.



(b) $b/a = 1.2$ and sharpened $b/a = 1.2$.



(c) $b/a = 1.4$ and flattened $b/a = 1.4$.



(d) $b/a = 1.5$ and flattened $b/a = 1.5$.

Figure 4.6: Squared normalized AFD coefficients of the Fundamental Mode for the original elliptical profiles, the corresponding locally modified geometries, and the $b/a = 1.3$ reference ellipse, evaluated at $F = 1.6$: (a) sharpened $b/a = 1.1$, (b) sharpened $b/a = 1.2$, (c) flattened $b/a = 1.4$, and (d) flattened $b/a = 1.5$.For each axis ratio, open and filled markers denote the original ellipse and the corresponding locally modified profile, respectively, while black crosses denote the $b/a = 1.3$ reference geometry.

4.5 Dielectric-Mode Cut-Off Frequencies

The effect of the local profile modification on the Dielectric-Mode cut-off frequencies is investigated using the isolated-tube model described in Section 3.2. The analysis considers the same EH-polarized $\nu = 2$ radial family examined in Chapter 3.

A direct comparison between each locally modified profile and its corresponding parent ellipse shows that the m–F_c sequences are almost unchanged by the local sharpening or flattening of the core-facing region. In particular, the modified profiles retain the distinct cut-off distributions associated with their original axis ratios.

To quantify the small residual differences, the cut-off frequency variation is defined as

$$\Delta F_c(m) = F_c^{\mathrm{mod}}(m) - F_c^{\mathrm{ell}}(m), \tag{4.7}$$

where F_c^{mod} and F_c^{ell} denote the cut-off frequencies of the locally modified profile and of the corresponding original ellipse, respectively.

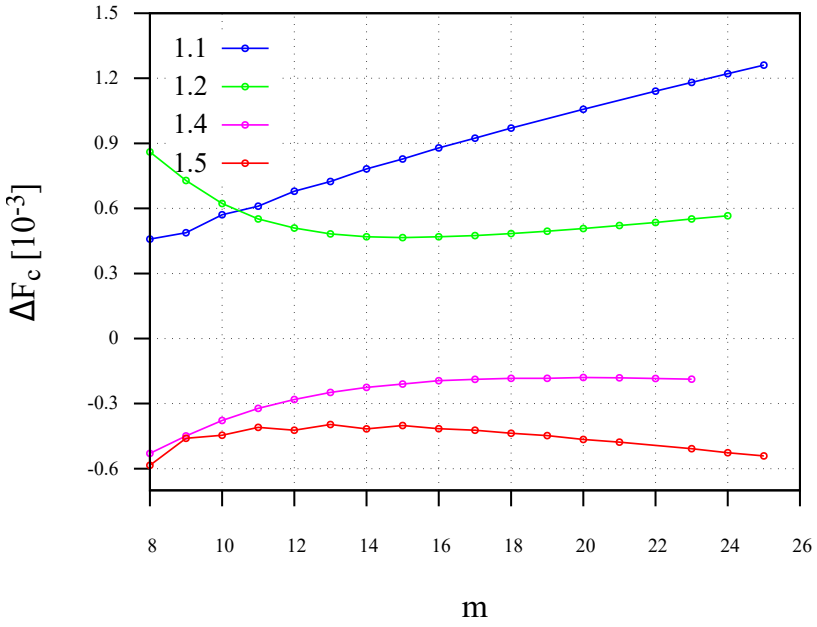


Figure 4.7: Difference between the normalized cut-off frequencies of the locally modified profiles and those of the corresponding original ellipses, $\Delta F_c = F_c^{\mathrm{mod}} - F_c^{\mathrm{ell}}$, for the EH-polarized Dielectric Modes of the $\nu = 2$ radial family in the azimuthal-order interval, $8 \leq m \leq 25$

Figure 4.7 confirms that the local profile modification produces only small shifts of the DM cut-off frequencies. Over the azimuthal-order interval shown, the largest absolute variation is approximately 1.26×10^{-3}, obtained for the sharpened $b/a = 1.1$ profile. The sharpened geometries exhibit small positive shifts, whereas the flattened

profiles exhibit small negative shifts, but in all cases the variations remain of the order of 10^{-3} or smaller. This limited displacement can be considered together with the small variation of the tube inner-boundary length produced by the local reshaping. With respect to the corresponding parent ellipses, the relative perimeter variations are -0.31%, -0.17%, $+0.63\%$, and $+1.04\%$ for the sharpened $b/a = 1.1$, sharpened $b/a = 1.2$, flattened $b/a = 1.4$, and flattened $b/a = 1.5$ profiles,respectively. The present results show that the local reshaping of the core-facing region, when accompanied by only a small variation of the total boundary length, produces only a limited perturbation of the DM spectral positions. This is consistent with the spatial-wavenumber analysis of Section 3.8, where the DM cut-off distributions were shown to be strongly organized by the global boundary scale.

4.6 Combined Interpretation of Mode-Coupling Loss

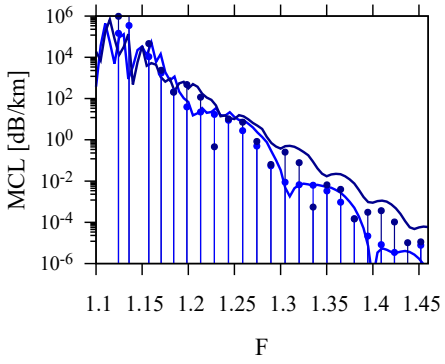
The previous analyses show that the local modification of the core-facing tube profile affects the two modal quantities involved in Mode-Coupling Loss differently. The Fundamental-Mode azimuthal spectrum undergoes a significant redistribution, whereas the Dielectric-Mode cut-off frequencies remain nearly unchanged with respect to the corresponding parent ellipse.

To combine these results, the same frequency-domain representation introduced in Section 3.7 is adopted. For each azimuthal order m, the squared normalized AFD coefficient $|\widetilde{R}_m|^2$ is positioned at the cut-off frequency $F_c(m)$ of the corresponding EH-polarized Dielectric Mode.

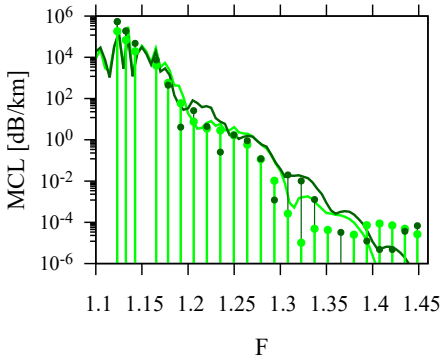
Figure 4.8 compares, for each parent ellipse, the MCL spectrum and the mapped AFD distribution before and after the local profile modification. The comparison is restricted to the same azimuthal-order interval, $8 \leq m \leq 25$, adopted in Chapter 3.

Since the local profile modification produces only small variations of the DM cut-off frequencies, the mapped contributions retain nearly the same spectral positions as those of the corresponding parent ellipses. The main effect of the modification is therefore a change in their relative weights, directly reflecting the redistribution of the Fundamental-Mode azimuthal spectrum described in Section 4.4.

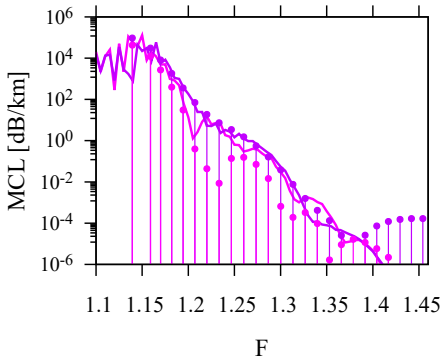
The comparison with the MCL spectra shows that the displacement of the falling edge toward the $b/a = 1.3$ reference observed for the modified $b/a = 1.2$, 1.4, and 1.5 profiles is consistent with the redistribution of the FM harmonic content available for interaction with the corresponding Dielectric Modes. The sharpened $b/a = 1.1$ profile remains the main exception, owing to the additional resonant structure introduced by the local modification.



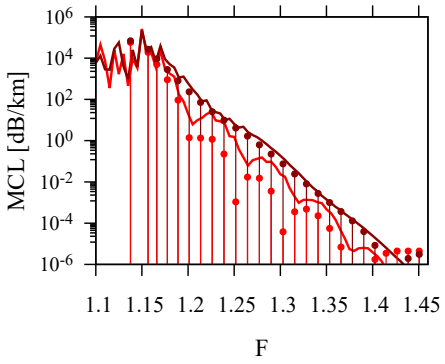
(a) $b/a = 1.1$ and sharpened $b/a = 1.1$.



(b) $b/a = 1.2$ and sharpened $b/a = 1.2$.



(c) $b/a = 1.4$ and flattened $b/a = 1.4$.



(d) $b/a = 1.5$ and flattened $b/a = 1.5$.

Figure 4.8: Mode-Coupling Loss spectra and mapped squared normalized AFD coefficients for the original elliptical profiles and the corresponding locally modified geometries. The coefficients are mapped onto the cut-off frequencies of the corresponding EH-polarized Dielectric Modes. Darker tones refer to the original ellipses, while the corresponding lighter tones refer to the locally modified profiles. The AFD distributions are independently rescaled for graphical comparison with the corresponding MCL spectra.

4.7 Conclusions

In this chapter, the effect of a local modification of the core-facing tube profile has been investigated while preserving the global dimensions associated with the corresponding parent ellipse. The modified geometries were designed so that their curvature distribution in the region surrounding the hollow-core-facing apex approaches that of the $b/a = 1.3$ reference profile.

The numerical results show that the local modification can produce a marked change in Mode-Coupling Loss while preserving the overall dimensions of the corresponding parent ellipse. This effect is particularly evident for the sharpened $b/a = 1.2$ and flattened $b/a = 1.5$ profiles, whose MCL falling edges move substantially toward the response of the $b/a = 1.3$ reference. The $b/a = 1.4$ case exhibits the same tendency starting from an already similar loss spectrum, whereas the sharpened $b/a = 1.1$ profile shows a more complex response characterized by additional resonant features.

The modal analysis provides an interpretation of this behavior. The local reshaping produces a significant redistribution of the Fundamental-Mode azimuthal spectrum, whereas the Dielectric-Mode cut-off frequencies remain very close to those of the corresponding parent ellipses. For the $b/a = 1.2$, 1.4, and 1.5 profiles, the redistribution of the relevant FM components accompanies the displacement of the MCL falling edge toward the $b/a = 1.3$ response, while the $b/a = 1.1$ profile retains a more irregular behavior.

Together with the results of Chapter 3, these findings show a different sensitivity of the two modal quantities to the tube geometry. The Dielectric-Mode cut-off distribution is strongly organized by the global curvilinear scale of the tube boundary, whereas the Fundamental-Mode azimuthal content retains a stronger dependence on the detailed shape of the core-facing profile.

Chapter 5

Conclusions

This thesis investigated how the shape of the cladding tubes affects Mode-Coupling Loss in Hollow-Core Inhibited-Coupling Fibers. An eight-tube Tube Lattice Fiber was considered, and the numerical analysis combined the Mode-Coupling Loss obtained from the complete fiber model with the Azimuthal Fourier Decomposition of the Fundamental Mode and the Dielectric-Mode cut-off frequencies calculated through an isolated-tube model. The analysis was aimed at understanding how global and local modifications of the tube profile affect the two modal quantities involved in the core–cladding interaction and, consequently, the MCL spectrum.

In Chapter 3, the influence of the global tube shape was investigated by considering the circular reference geometry and elliptical profiles with progressively increasing axis ratio. The resulting MCL falling edge was found to evolve non-monotonically with the tube axis ratio. In particular, at the reference level of 10^{-2} dB/km adopted for the comparison, the $b/a = 1.3$ geometry exhibits the lowest-frequency crossing among the investigated profiles. The modal analysis shows that this behavior cannot be attributed to either the FM azimuthal spectrum or the DM cut-off distribution alone. Ellipticity produces a non-uniform redistribution of the FM Fourier components, while, as the axis ratio and the corresponding tube perimeter increase, the EH Dielectric-Mode cut-off sequence shifts toward lower normalized frequencies and becomes progressively compressed. The combined AFD–cut-off representation provides the spectral information required to interpret these changes by associating the relative FM harmonic content with the approximate spectral positions of the corresponding DM interactions. The subsequent spatial-wavenumber analysis further shows that a substantial part of the displacement of the DM cut-off sequences is associated with the change in the global curvilinear scale of the tube boundary. When the azimuthal order is expressed through the boundary spatial wavenumber $k_s = 2\pi m/P$, the cut-off sequences of the different elliptical geometries become strongly aligned, while the FM azimuthal spectra retain significant shape-dependent differences.

In Chapter 4, the role of the core-facing tube region was investigated more directly. Starting from different parent ellipses, the boundary surrounding the tube apex was locally sharpened or flattened so that its curvature distribution approached that of the $b/a = 1.3$ reference profile, while preserving the global dimensions associated with the parent geometry. These local modifications were sufficient to produce marked changes in MCL. The effect is particularly evident for the sharpened $b/a = 1.2$ and flattened $b/a = 1.4$, $b/a = 1.5$ profiles, whereas the sharpened $b/a = 1.1$ case exhibits a more complex response with additional resonant features. A different response of the two modal quantities emerges from this local analysis. The core-facing reshaping can substantially redistribute the FM azimuthal content, whereas the corresponding DM cut-off sequences remain very close to those of the parent ellipses. The observed modification of the MCL falling edge is therefore not accompanied by a comparable displacement of the Dielectric-Mode cut-off distribution, but is consistent with a redistribution of the FM azimuthal components available for interaction with the corresponding DMs.

Taken together, the global and local investigations reveal a different sensitivity of the two modal quantities to the tube shape. The Dielectric-Mode cut-off distribution is strongly organized by the global curvilinear scale of the tube boundary, while the Fundamental-Mode azimuthal content retains a stronger dependence on the detailed shape of the core-facing profile. These results do not establish a one-to-one relation between local curvature and Mode-Coupling Loss, which remains determined by the complete core–cladding modal interaction. They identify, however, the local core-facing tube profile as an additional geometrical degree of freedom through which the FM azimuthal content, and consequently the Mode-Coupling Loss, can be modified without substantially altering the Dielectric-Mode cut-off distribution.

Further developments could first address a complete Coupled-Mode-Theory description of the FM–DM interactions. The calculation of the coupling coefficient, propagation-constant mismatch, and differential attenuation for each interacting mode pair would allow the individual resonance contributions to be reconstructed quantitatively. A complementary extension would be to evaluate selected tube shapes without the artificial-index material, in order to assess how the modifications of Mode-Coupling Loss identified here combine with the Tube-Tunneling-Loss contribution in the complete Confinement Loss.

Bibliography

[1] E. Numkam Fokoua, S. A. Mousavi, G. T. Jasion, D. J. Richardson, and F. Poletti, "Loss in hollow-core optical fibers: Mechanisms, scaling rules, and limits," *Advances in Optics and Photonics*, vol. 15, no. 1, pp. 1–85, 2023.

[2] L. Vincetti and V. Setti, "Waveguiding mechanism in tube lattice fibers," *Optics Express*, vol. 18, no. 22, pp. 23 133–23 146, 2010.

[3] F. Melli, L. Rosa, K. Vasko, F. Benabid, and L. Vincetti, "Analytical framework for mode-coupling in hollow-core inhibited-coupling fibers," *Journal of Lightwave Technology*, vol. 43, no. 11, pp. 5464–5472, 2025.

[4] F. Melli, L. Rosa, K. Vasko, F. Benabid, and L. Vincetti, "Disentangling loss mechanisms to bridge inhibited-coupling and anti-resonant models in hollow-core fibers," *Journal of Lightwave Technology*, vol. 44, no. 11, pp. 4714–4724, 2026.

[5] L. Rosa, F. Melli, and L. Vincetti, "Analytical formulas for dispersion and effective area in hollow-core tube lattice fibers," *Fibers*, vol. 9, no. 10, p. 58, 2021.

[6] L. Vincetti and L. Rosa, "A simple analytical model for confinement loss estimation in hollow-core tube lattice fibers," *Optics Express*, vol. 27, no. 4, pp. 5230–5237, 2019.

[7] F. Melli, K. Vasko, L. Rosa, F. Benabid, and L. Vincetti, "Azimuthal fourier decomposition for loss analysis of hollow-core tube lattice fibers part i: Ideal fibers," *Results in Optics*, vol. 15, p. 100 657, 2024.

[8] B. Debord et al., "Ultralow transmission loss in inhibited-coupling guiding hollow fibers," *Optica*, vol. 4, no. 2, pp. 209–217, 2017.

[9] L. Vincetti, "Empirical formulas for calculating loss in hollow core tube lattice fibers," *Optics Express*, vol. 24, no. 10, pp. 10 313–10 325, 2016.

[10] K. Okamoto, *Fundamentals of Optical Waveguides*, 2nd ed. Academic Press, 2006, ISBN: 978-0-12-525096-2.

[11] F. Couny, F. Benabid, P. J. Roberts, P. S. Light, and M. G. Raymer, "Generation and photonic guidance of multi-octave optical-frequency combs," *Science*, vol. 318, no. 5853, pp. 1118–1121, 2007.

[12] L. Vincetti and V. Setti, "Extra loss due to fano resonances in inhibited coupling fibers based on a lattice of tubes," *Optics Express*, vol. 20, no. 13, pp. 14 350–14 361, 2012.

[13] T. Birks, P. Roberts, P. Russell, D. Atkin, and T. Shepherd, "Full 2-d photonic bandgaps in silica/air structures," *Electronics Letters*, vol. 31, no. 22, pp. 1941–1943, 1995.

[14] D. Marcuse, *Theory of Dielectric Optical Waveguides*, 2nd ed. Academic Press, 1991.

[15] L. Yang, L.-L. Xue, Y.-C. Lu, and W.-P. Huang, "New insight into quasi leaky mode approximations for unified coupled-mode analysis," *Optics Express*, vol. 18, no. 20, pp. 20 595–20 609, 2010.

[16] W.-P. Huang and J. Mu, "Complex coupled-mode theory for optical waveguides," *Optics Express*, vol. 17, no. 21, pp. 19 134–19 152, 2009.

[17] Z. Zhang, Y. Shi, B. Bian, and J. Lu, "Dependence of leaky mode coupling on loss in photonic crystal fiber with hybrid cladding," *Optics Express*, vol. 16, no. 3, pp. 1915–1922, 2008.

[18] C. W. Hsu, B. Zhen, A. D. Stone, J. D. Joannopoulos, and M. Soljačić, "Bound states in the continuum," *Nature Reviews Materials*, vol. 1, no. 9, p. 16 048, 2016.

[19] M. Kharadly and J. Lewis, "Properties of dielectric-tube waveguides," *Proceedings of the Institution of Electrical Engineers*, vol. 116, pp. 214–224, 1969.

[20] E. A. J. Marcatili and R. A. Schmeltzer, "Hollow metallic and dielectric waveguides for long distance optical transmission and lasers," *Bell System Technical Journal*, vol. 43, no. 4, pp. 1783–1809, 1964.

[21] F. Melli, F. Giovanardi, K. Vasko, L. Rosa, F. Benabid, and L. Vincetti, "Azimuthal fourier decomposition for loss analysis of hollow-core tube lattice fibers part ii: Tube thickness variation effects," *Results in Optics*, vol. 16, p. 100 726, 2024.

[22] F. Poletti, "Nested antiresonant nodeless hollow core fiber," *Optics Express*, vol. 22, no. 20, pp. 23 807–23 828, 2014.

[23] M. Duguay, Y. Kokubun, T. L. Koch, and L. Pfeiffer, "Antiresonant reflecting optical waveguides in sio2-si multilayer structures," *Applied Physics Letters*, vol. 49, no. 1, pp. 13–15, 1986.

[24] W. Ding and Y. Wang, "Analytic model for light guidance in single-wall hollow-core anti-resonant fibers," *Optics Express*, vol. 22, no. 22, pp. 27 242–27 256, 2014.

[25] P. Song, K. Y. Phoong, and D. Bird, "Quantitative analysis of antiresonance in single-ring, hollow-core fibres," *Optics Express*, vol. 27, no. 20, pp. 27 745–27 760, 2019.

[26] L. R. Murphy and D. Bird, "Azimuthal confinement: The missing ingredient in understanding confinement loss in antiresonant, hollow-core fibers," *Optica*, vol. 10, no. 7, pp. 854–870, 2023.

[27] D. Bird, "Attenuation of model hollow-core, anti-resonant fibres," *Optics Express*, vol. 25, no. 19, pp. 23 215–23 237, 2017.